Integrative *in vivo* analysis of the ethanolamine utilization bacterial microcompartment in *Escherichia coli*.

Running title: *In vivo* functionality of the *E. coli* Eut BMC

Denis Jallet[1#], Vanessa Soldan[2], Ramteen Shayan[2], Alexandre Stella[3,5], Nour Ismail[1], Rania Zenati[1], Edern Cahoreau[1,4], Odile Burlet-Schiltz[3,5], Stéphanie Balor[2], Pierre Millard[1,4], Stéphanie Heux[1].

[1] Toulouse Biotechnology Institute, Université de Toulouse, CNRS, INRAE, INSA, Toulouse, France

[2] Plateforme de Microscopie Electronique Intégrative, Centre de Biologie Intégrative, Université de Toulouse, CNRS, Toulouse, France

[3] Institut de Pharmacologie et de Biologie Structurale (IPBS), Université de Toulouse, CNRS, Université Toulouse III – Paul Sabatier (UT3), Toulouse, France

[4] MetaToul-MetaboHUB, National infrastructure of metabolomics and fluxomics, Toulouse, France

[5] Infrastructure nationale de protéomique, ProFI, FR 2048, Toulouse, France

Correspondance: denis.jallet@insa-toulouse.fr

Abstract

Bacterial microcompartments (BMCs) are self-assembling protein megacomplexes that encapsulate metabolic pathways. Although approximately 20% of sequenced bacterial genomes contain operons encoding putative BMCs, few have been thoroughly characterized, nor any in the most studied *Escherichia coli* strains. We used an interdisciplinary approach to gain deep molecular and functional insights into the ethanolamine utilization (Eut) BMC system encoded by the *eut* operon in *E. coli* K-12. The *eut* genotype was linked with the ethanolamine utilization phenotype using deletion and overexpression mutants. The subcellular dynamics and morphology of the *E. coli* Eut BMC were characterized *in cellula* by fluorescence microscopy and electron (cryo)microscopy. The minimal proteome reorganization required for ethanolamine utilization and the *in vivo* stochiometric composition of the Eut BMC were determined by quantitative proteomics. Finally, the first flux map connecting the Eut BMC with central metabolism *in cellula* was obtained by genome scale modelling and ^{13}C-fluxomics. Our results reveal that, contrary to previous suggestions, ethanolamine serves both as a nitrogen and a carbon source in *E. coli* K-12, while also contributing significant metabolic overflow. Overall, this study provides a quantitative molecular and functional understanding of the BMCs involved in ethanolamine assimilation by *E. coli*.

Importance

The properties of BMCs make them an ideal tool to build orthogonal network structures with minimal interactions with native metabolic and regulatory networks. However, this requires an understanding of how BMCs work natively. In this study, we combined genetic manipulation, multi-omics, modelling and microscopy to address this issue for Eut BMCs. We show that the Eut BMC in *E. coli* turns ethanolamine into usable carbon and nitrogen substrates to sustain growth. These results improve our understanding of compartmentalization in a widely used bacterial chassis.

Introduction

Compartmentalization was initially considered a defining feature of eukaryotic cells. With the advent of transmission electron microscopy (TEM) however, subcellular structures were also discovered in bacteria, including bacterial microcompartments (BMCs) such as carboxysomes in certain autotrophic taxa[1]. Genes encoding for BMC shell proteins were subsequently discovered in heterotrophic taxa[2,3] and recent isolate and metagenomics data suggest that roughly 20% of bacteria have BMC encoding operons[4]. These genes are generally found in large operons with the other genetic components required to produce BMCs, often referred to as metabolosomes, because of their typically catabolic rather than anabolic function. The ethanolamine utilization (Eut) BMC in *Salmonella enterica* was one of the first studied metabolosome systems[5].

Ethanolamine (EA) accumulates in mammalians' gastrointestinal and urinary tracts upon degradation of phosphatidylethanolamine. EA utilization confers competitive advantages to certain pathogenic bacteria in the gut environment[6–8]. Some *Escherichia coli* strains can utilize EA as sole nitrogen and carbon source in the presence of vitamin B12[6,9–12]. EA utilization was initially thought to be associated with pathogenicity[6,13] but several commensal *E. coli* strains also metabolize EA[11,12]. The *E. coli* core genome natively hosts a 17-gene *eut* operon (*eutSPQTDMNEJGHABCLKR*) with strong homology to the *eut* operon of *S. enterica*[14,15]. Other genes, such as *maeB, talA or tktB*, flank the *eut* operon to form an extended EUT1 locus[16,17]. The EUT1 locus is well conserved amongst various Beta- and Gammaproteobacteria[4], suggesting a functional link between at least some of these ancillary EUT1 proteins and EA utilization[16]. However, the link has not been evaluated experimentally yet. EUT loci with different *eut* operon arrangements and ancillary gene contents also exist amongst bacteria (i.e. EUT2 and EUT3 loci[4,16]). Since *E. coli* only has an EUT1 locus, EUT1 will be the focus of the present study.The *eut* operon contains genes encoding for BMC components. The Eut BMC shell is made up of ring-shaped oligomeric proteins (EutSMNLK), some of which have central pores that allow some small metabolites to pass, including EA and its degradation products[18]. Inside Eut BMCs, EA is thought to be deaminated into acetaldehyde plus ammonium (NH_4) by EAL (EutBC), but the exact metabolic topology involved remains debated[19,20]. Acetaldehyde is further converted through enzymatic reactions. NH_4, ethanol and acetyl-P would eventually diffuse out through the shell to be used in central metabolism or excreted[19]. But again, the exact BMC core protein complement remains hypothetical. Two Eut enzymes (EutC, EutE) bear encapsulation peptides that likely favour their internalization[21,22]. Other Eut enzymes may form complexes or interact with shell components.

Electron micrographs of *E. coli* Eut BMCs have only ever been reported twice[9,23]. Indeed, while irregular polyhedral structures with a diameter of around 100 nm can be observed in *E. coli* K-12 and *E. coli* UPEC U1 after *eut* induction, it is unclear whether these Eut BMCs are well formed and functionally required for EA catabolism. Intact Eut BMCs have never been purified to date, either from *E. coli* or from *S. enterica*, and our knowledge of these systems mainly comes from genetic studies in *S. enterica*[19,20,24] and *in vitro* structural and functional characterizations of individual recombinant Eut proteins[18].

Overall, Eut BMCs play a safeguarding role by sequestering and favouring the downstream conversion of toxic and volatile acetaldehyde intermediates[20]. Their spatial arrangement favours metabolic channelling and it has been reported that compartmentalisation may increase catalytic activity by up to 6-fold compared with non-compartmentalised reactions[25]. Another advantage is that the cofactors required for enzyme activity are regenerated within the BMC thus limiting competition with enzymes from the cytosol[19]. These properties make Eut BMCs and BMCs interesting metabolic units for biotechnological applications[26], but a better understanding of their regulation, assembly and function is still required to make them amenable to engineering. With these knowledge gaps in mind, we

83 performed a systemic analysis from the molecular to the functional level of native BMC-mediated EA
84 catabolism in *E. coli* K-12. We characterized wild-type (WT) *E. coli* K-12 W3110 and several mutant
85 strains by epifluorescence microscopy, TEM and electron cryotomography (cryoET) and performed a
86 multi omics analysis to understand how BMC-mediated EA utilization affects bacterial physiology.

87 **Results**

88 *1) Necessity of the eut operon for EA utilization.*

89 The EUT1 locus of *E. coli* K-12 W3110 (Fig.1A) is similar in gene content to *S. enterica* LT2's, with more
90 than 73 % primary structure identity between individual EUT1 proteins from the two species (Table
91 S2). In contrast, the *eut* operon of *E. coli* K-12 BW25113 is natively interrupted by a prophage DNA
92 insertion downstream of *eutA* (Fig.S1A). *E. coli* K-12 does not contain any other putative BMC locus
93 besides EUT1 (e.g. no PDU locus). To investigate the link between *eut* genotype and EA catabolism, we
94 first constructed several mutant strains by genome editing[27]. The *eut* operon was knocked out from
95 WT W3110 to yield W3110 Δ*eut* (Table 1; Fig.S1B). The prophage DNA insertion in BW25113 WT was
96 scarlessly removed to reconstitute an intact *eut* operon, thereby generating BW25113 *eut+*. We
97 additionally built *eut* overexpressors by cloning the entire W3110 WT *eut* operon downstream of an
98 IPTG-inducible promoter (P_{trc}[28]) in pSEVA661[29], yielding pEut (Fig.S1C). pEut was transformed into
99 W3110 Δ*eut* for complementation assays.

100 Growth experiments were performed using a microplate reader to evaluate each strain's EA utilization
101 capacity. The W3110 strains (WT and Δ*eut*) behaved similarly in control M9 medium with glycerol as C
102 source and NH_4Cl as N source (Fig.1B). However, only the WT strain grew in M9 glycerol EA B12, where
103 EA was the only available N source (Fig.1C). W3110 WT had comparable growth rates (Table 2) but
104 significantly higher OD_{600nm} after 24 h in M9 glycerol EA B12 than in M9 glycerol NH_4Cl (0.73 ± 0.01 VS
105 0.56 ± 0.04). BW25113 WT behaved like W3110 Δ*eut* and BW25113 *eut+* behaved like W3110 WT
106 (Fig.S1D-E), indicating that an uninterrupted *eut* operon is essential for EA utilization as N source. Note
107 that none of the strains grew in M9 EA B12 where EA was the only available N and C source (Fig.S1F).
108 In M9 glycerol NH_4Cl with gentamicin (Gm), W3110 Δ*eut* pEut's growth rate was similar to that of the
109 empty-vector control (W3110 Δ*eut* pO) and of the corresponding plasmid-bearing WT derivatives
110 (Table 2; Fig.1B). W3110 Δ*eut* pO did not grow in M9 glycerol EA B12 Gm (Fig.1C) while W3110 Δ*eut*
111 pEut utilized EA as sole N source with a maximal growth rate similar to that of W3110 WT pO (Table 2)
112 but with a markedly lower final OD_{600nm} (0.60 ± 0.01 VS 0.77 ± 0.01). The W3110 *eut* phenotype was
113 thus at least partially recovered in the plasmid construct, even without IPTG induction, which indicates
114 that the P_{trc} promoter is leaky. When 20 µM IPTG was added at culture initiation, W3110 WT pEut and
115 W3110 Δ*eut* pEut had significantly lower growth rates than the empty vector controls in both M9
116 glycerol NH_4Cl Gm and M9 glycerol EA B12 Gm (Fig.1D,E; Table 2). These results show that *eut*
117 expression levels must be kept low to avoid any negative impact on growth and enable efficient EA
118 utilization.

119 *2) Subcellular localization of the EutC enzyme.*

120 The EUT1 locus encodes a functional EA utilization pathway but does it truly drive the production of
121 Eut BMCs *in cellula*? We first attempted to visualize *E. coli* Eut BMCs by fluorescence microscopy and
122 EutC-GFP fusion. We focused on EutC because it natively carries a 20 amino-acid long N-terminal
123 peptide (referred to as $EutC_{1-20}$ hereafter) that should ensure its encapsulation within BMCs[21,22]. To
124 keep expression levels low, the synthetic gene was inserted at the SS9 safe chromosomal locus[30] (Table
125 1; Fig2A) in W3110 WT under the control of an anhydrotetracycline (aTc) inducible promoter ($P_{LtetO-1}$[31]).
126

127 No GFP fluorescence emission was detected in the absence of aTc (Fig.S2A). In M9 glycerol NH_4Cl with
128 8 ng.ml^{-1} aTc, a faint cytosolic GFP signal was observed (Fig.2B). In M9 glycerol EA B12 with 8 ng.ml^{-1}
129 aTc, multiple GFP puncta were observed moving rapidly around the cytosol (Fig.2C; Movie S1; wider
130 views in Fig.S3). These mobile GFP puncta are similar to those visualized by fluorescence microscopy
131 for the *S. enterica* Eut BMC system[21,32]. There were 5.9 ± 1.1 GFP puncta per bacterium on average, a
132 number that did not vary significantly upon increasing the aTc concentration up to 80 ng.ml^{-1} (6.3 ±
133 1.2) (Fig.2D,E). To investigate whether EutC$_{1-20}$ alone could drive the encapsulation of a heterologous
134 protein, we also built a smaller cassette expressing the EutC$_{1-20}$-GFP fusion protein (Fig.S2B). W3110
135 *eutC$_{1-20}$-GFP* behaved like W3110 *eutC-GFP* but with a stronger cytosolic GFP background (Fig.S2C-E),
136 making it harder to distinguish the puncta. The diffuse GFP background in W3110 *eutC$_{1-20}$-GFP* likely
137 came from non-encapsulated EutC$_{1-20}$-GFP fusions.

138 *3) Morphology of Eut BMCs in cellula.*

139 We first used a traditional TEM-based approach to evaluate the integrity of the Eut BMCs *in cellula*. No
140 BMC-like structure was detected in W3110 WT growing in M9 glycerol NH_4Cl (Fig.S4A). In M9 glycerol
141 EA B12, irregular polyhedral assemblies roughly 100 nm in diameter, with sharp edges and a well-
142 defined delimiting layer were observed in some slices (Fig. S4B). Since these assemblies satisfy the
143 morphological criteria for BMCs[33] we refer to them hereafter as Eut BMCs. These were present in about
144 1 in 50 bacterial slices. On LB medium supplemented with EA and vitamin B12 to induce *eut*, Eut BMCs
145 were detected in about 1 in 10 bacterial slices (Fig.S4C) suggesting that more BMCs were present.
146 Finally, W3110 Δ*eut* pEut was cultivated in LB containing IPTG to strongly induce the *eut* operon
147 expression. Here, BMCs with various polyhedral geometries and dimensions were observed in most
148 bacteria (Fig.S4D). Increasing the *eut* operon expression strength thus increased the number of BMCs
149 per bacterium but had a negative effect on growth.

150 CryoET reconstructions of W3110 WT grown in M9 glycerol EA B12 revealed several cellular features
151 including the inner and outer membranes, ribosomes, and Eut BMCs (Fig.3A-B). Multiple Eut BMCs
152 were observed per bacterium, surrounded by a thin layer (the BMC shell) with sharp edges and vertices
153 (Fig.3C-D). The shell often completely enclosed the core but structures resembling partial Eut BMCs
154 were also present (arrow in Fig.3D). Further experiments are required to determine whether these
155 apparently partial Eut BMCs correspond to (dis)assembling states or are in fact cryoET (e.g. missing
156 wedge) artefacts. The Eut BMC core was somewhat granular in appearance but more electron dense
157 than the surrounding cytoplasm, with several encapsulated components, likely proteins. This was
158 particularly apparent in bacteria with a clear cytosol after partial lysis (Fig.3D). Overall, these *E. coli* Eut
159 BMCs were more heterogenous in size and shape than cyanobacterial carboxysomes[34]. Tomograms of
160 the W3110 Δ*eut* pEut strain cultivated in M9 glycerol EA B12 Gm IPTG as a control showed a higher
161 number of Eut BMCs per bacterium compared with the WT (Fig.3E-F; Fig.S5), but with similar shapes
162 and dimensions. These first ever cryoET images of Eut BMCs in a bacterium demonstrate that native *E.*
163 *coli* Eut BMCs are properly formed.

164 *4) EA utilization requires minimal reorganization of the proteome.*

165 Since Eut BMCs are protein-based, we investigated how their production affects *E. coli* using label-free
166 quantitative mass spectrometry-based proteomics. Samples were collected and compared between
167 exponentially growing cultures of W3110 WT maintained aerobically in M9 glycerol EA B12 versus M9
168 glycerol NH_4Cl. Of the 1999 quantifiable proteins, only 48 were significantly more abundant and 8 less
169 abundant in M9 glycerol EA B12 compared with M9 glycerol NH_4Cl (Fig.4A; Table S3). Two distinct
170 modules were identified among these proteins by interaction network analysis using STRING v11.5[35]
171 (Fig.4B).

172 Some of the *eut* encoded proteins in the first module were detected in M9 glycerol EA B12 only
173 (EutHNPR), while the others were barely detectable in M9 glycerol NH_4Cl and strongly upregulated in
174 M9 glycerol EA B12, with fold changes ranging from 5 (EutJ) to 325 (EutM) (Fig.4A). This included
175 enzymes linked to EA catabolism (EutAPQDEGBC) and the structural Eut BMC shell components
176 (EutSMNLK). We calculated the abundance of each Eut protein in M9 glycerol EA B12 corrected for the
177 number of theoretically observable tryptic peptides (iBAQ values[36]: Fig.4C), to correct for differences
178 in molecular weight and amino-acid sequences. Relative to the most abundant protein, EutQ, an
179 acetate kinase[37], whose relative abundance was set to 100, the most abundant predicted shell
180 components were EutM, EutL, EutS, EutK and EutN with relative abundances of 96 ± 14, 39 ± 1, 11 ± 3,
181 8 ± 1, and 1 ± 1, respectively. The most abundant putative Eut BMC core enzymes besides EutQ were
182 EutB, EutE, EutC, EutD, EutG and EutP (a second acetate kinase), with relative abundances of 37 ± 17,
183 27 ± 10, 24 ± 9, 10 ± 3, 7 ± 1 and 7 ± 1, respectively.

184 Eleven ancillary proteins are encoded within the EUT1 locus[4,16] (Fig.1A, Table S2). We could quantify 7
185 of them: the transketolase TktB, the transaldolase TalA, the malic enzyme MaeB, the N-
186 acetylmuramoyl-L-alanine amidase AmiA, the putative acetyl-transferase YpeA, the protein of
187 unknown function YfeY as well as the porphyrinogen oxidase YfeX (Table S4). None of these proteins
188 were differentially accumulated in M9 glycerol EA B12 compared to M9 glycerol NH_4Cl. Distinct
189 regulatory mechanisms therefore control their production as compared to the *eut* operon encoded
190 elements, i.e. the presence of EA and vitamin B12 does not induce the accumulation of the ancillary
191 proteins. The remaining ancillary EUT1 proteins were not detected, possibly because of low expression
192 levels or a high hydrophobicity precluding their extraction/identification.

193 The second identified module consisted of proteins involved in maintaining intracellular N homeostasis
194 (Fig.4B), a majority of which were more highly expressed in M9 glycerol EA B12, including the
195 ammonium transporter AmtB, its cognate regulator GlnK and a two-component system (GlnG-GlnL)
196 controlling N assimilation[38,39]. The second module also contained enzymes catalysing (de)amination
197 reactions, such as asparagine synthetase (AsnAB), succinylglutamate semialdehyde dehydrogenase
198 (AstCD), glutamine synthetase (GlnA), and guanine deaminase (GuaD). Proteins involved in the uptake
199 of extracellular dipeptides (DdpAX), polypeptides (OppA) and amino acids (ArgT, CycA, HisQ) were also
200 present. Several regulators and pathways normally mobilized under N starvation conditions were
201 therefore activated in M9 glycerol EA B12, probably due to the absence of extracellular N sources other
202 than EA. Note that the abundance of cobalamin-independent homocysteine transmethylase (MetE)
203 was 7 times lower in M9 glycerol EA B12 than in M9 glycerol NH_4Cl. MetE normally participates in
204 methionine biosynthesis but it can be replaced by MetH (cobalamin-dependent methionine synthase)
205 in the presence of vitamin B12[40]

206 Overall, these results indicate that the production of Eut BMCs did not have a pleiotropic effect, since
207 only proteins involved in BMC synthesis and N metabolism were affected.

208 *5) Analysis of EA utilization by exometabolomics.*

209 To decipher the metabolic functioning of the Eut BMCs, we grew W3110 WT under aerobic conditions
210 in M9 derivatives containing glycerol as C source and either EA or NH_4Cl as N source (Fig.S6A-B).
211 Cyanocobalamin was again added to the EA-containing medium. The cultures reached similar maximal
212 growth rates in both media (Table 3) but the biomass concentration after 12 h was higher with EA than
213 with NH_4Cl (0.97±0.01 $g_{DW}.L^{-1}$ VS 0.72±0.01 $g_{DW}.L^{-1}$).

214 The exometabolome was analysed by ^{1}H-NMR and extracellular uptake and production fluxes were
215 calculated from these data using PhysioFit[41] (Table 3; Fig.S6C-D). With NH_4Cl as sole N source, glycerol
216 was fully assimilated and no by-products were detected. With EA as sole N source, glycerol was

217 consumed at a similar rate and EA was assimilated at a rate of 7.8 ± 0.3 mmol.g_{DW}^{-1}.h^{-1}. Ethanol ($q_{P)EtOH}$
218 = 2.6 ± 0.1 mmol.g_{DW}^{-1}.h^{-1}) and acetate ($q_{P)Ace}$ = 1.7 ± 0.1 mmol.g_{DW}^{-1}.h^{-1}) were excreted, and the acetate
219 was re-consumed upon exhaustion of glycerol and EA, explaining the higher final biomass under this
220 condition. Trace amounts of acetaldehyde were also detected, suggesting that some acetaldehyde
221 leaked from the Eut BMCs and escaped from the cells. Acetate, ethanol and acetaldehyde could all
222 result from EA catabolism[20]. Assuming NADH is recycled within the Eut BMCs, acetate and EtOH should
223 be produced in similar amounts[19]. Since the production rate of EtOH was significantly higher than that
224 of acetate during exponential growth, this suggests either that some of the EA-derived acetate was
225 used by cellular processes or that some of the EtOH was produced within the cytosol.

226 *6) Genome-scale predictions of EA utilization by E. coli.*

227 We next performed flux balance analysis (FBA[42]) on the same data to study the fate of EA in the Eut
228 BMC and cytosol. We adapted the genome scale model (GSM) of *E. coli* iML1515[43] by
229 compartmentalizing EA catabolism inside Eut BMCs, thereby ensuring that NADH and CoA-SH cofactors
230 are recycled within the BMCs, while ATP is recycled in the cytosol (Fig.S7). The model was then
231 constrained with the experimentally measured extracellular fluxes, assuming acetate and EtOH are
232 produced in the BMCs. When maximizing biomass production, the maximal FBA-predicted growth rate
233 was 0.72 h^{-1}. This value is higher than observed experimentally, indicating that glycerol and EA
234 utilization are suboptimal *in vivo*. We therefore constrained the growth rate to the experimental value
235 (Table 3: 0.45 h^{-1}) and defined ATP maintenance as the objective function[44] (Fig.S7). We also carried
236 out flux variability analysis (FVA) to identify the optimal solution and the range of fluxes that each
237 reaction can carry while maintaining at least 99 % of the objective.

238 The model predicted that Eut BMCs produce and release equimolar quantities of acetaldehyde,
239 ethanol and acetyl-P into the cytosol, each accounting for 33 % of the C from EA (Fig.S7). Acetaldehyde
240 can potentially escape from the cytosol into the extracellular medium, as reported previously[20], and/or
241 be utilized in metabolism. All the ethanol is excreted. Some of the acetyl-P is converted into acetate
242 (21 % of the C from EA) before excretion while the remaining portion can be converted into acetyl-CoA
243 to fuel anabolism and thereby support growth (12 % of the C from EA) (Fig.S7). While EA is thought to
244 act only as a nitrogen source for *E. coli* K-12, genome-scale modelling thus predicts that it may also
245 provide carbon. Moreover, the model indicates that the amount of EA-derived ammonium exceeds
246 the N needs of *E. coli* for growth, and a metabolic steady state can thus only be achieved if some of
247 the ammonium (38 % of the N from EA) is excreted.

248 *7) ^{13}C-metabolic flux analysis of EA and glycerol co-metabolism*

249 To test the predictions of the GSM, we performed a ^{13}C-metabolic flux analysis of W3110 WT grown in
250 M9 medium containing $^{12}C_3$-glycerol,$^{13}C_2$-EA as well as cyanocobalamin (Fig.5) and quantified the time-
251 course concentrations of labelled and unlabelled EtOH and acetate by ^{1}H-NMR (Fig.5A-B). EtOH was
252 virtually fully labelled (4.66 ± 0.44 mM $^{13}C_2$-EtOH VS 0.47 ± 0.03 mM $^{12}C_2$-EtOH after 10 h, Fig.5B),
253 demonstrating that about 90 % was produced from EA. The residual $^{12}C_2$-EtOH may have come either
254 from incomplete encapsulation of Eut enzymes (e.g. EutE converting cysotolic $^{12}C_2$-acetyl-CoA into $^{12}C_2$-
255 acetaldehyde and EutG, yielding $^{12}C_2$-EtOH), from cytosolic acetyl-CoA (produced from unlabelled
256 glycerol) entering misassembled BMCs, or from weak cytosolic conversion of glycerol to ethanol
257 through alternative cytosolic pathways. In contrast, only half of the acetate pool was labelled,
258 indicating that EA and glycerol contributed equally to acetyl-P synthesis and thus to acetate
259 production. The extracellular ammonium concentration, measured by ^{1}H-NMR, increased from 0.4 ±
260 0.1 mM after 3 h to 4.4 ± 0.1 mM after 11 h (Fig.5B).

261 Finally, we built a dynamic isotopic model to quantify *in vivo* fluxes within and around the Eut BMCs
262 by fitting the dynamics of all (labelled and unlabelled) exometabolites (Fig.5C; Table S5). This model
263 includes a coarse-grained representation of glycolytic conversion of glycerol to acetyl-P and of the
264 conversion of acetyl-P into acetate or its utilization elsewhere in metabolism for biomass synthesis, as
265 suggested by the GSM. This model fit the data satisfactorily (Fig.S8), supporting the validity of the
266 assumed network topology. Here, the Eut BMCs released more ethanol (Table S5; v_{EutG} = 2.7 ± 0.1
267 mmol.g_{DW}^{-1}.h^{-1}, 37% of the C from EA) and acetyl-P (v_{EutD} = 2.7 ± 0.1 mmol.g_{DW}^{-1}.h^{-1}, 37% of the C from
268 EA) than acetaldehyde ($v_{BMC)acetaldehyde}$ = 1.7 ± 0.1 mmol.g_{DW}^{-1}.h^{-1}, 26% of the C from EA). Consistent with
269 the labelling data, glycerol and EA contributed equally to the cytosolic acetyl-P pool (with $v_{Glycolysis}$ = 2.5
270 ± 0.1 mmol.g_{DW}^{-1}.h^{-1}). About 32 % of the acetyl-P pool was excreted as acetate ($q_{P)Acetate}$ = 1.6 ± 0.1
271 mmol.g_{DW}^{-1}.h^{-1} ; 12% of the C from EA) and the rest fuelled growth (v_{Pta} = 3.5 ± 0.1 mmol.g_{DW}^{-1}.h^{-1} ; 25%
272 of the C from EA). To confirm the significant anabolic utilization of carbon derived from EA, we
273 measured the carbon isotopologue distributions of proteinogenic amino acids (Fig.5D). In keeping with
274 the high ^{13}C-enrichment of the cytosolic acetyl-P pool (and therefore also the acetyl-CoA pool)
275 predicted by the isotopic model (Fig.S9), amino acids derived from the TCA cycle (i.e. Arg, Glu, Asp,
276 Thr, Lys, Ile) had high fractions of heavy isotopologues. In contrast, amino acids produced from
277 intermediates of the glycolytic and pentose phosphate pathways (i.e. Gly, Ser, His, Tyr, Phe, Ala, Val)
278 had much lower ^{13}C enrichment, pointing to an absence of neoglucogenic flux under the investigated
279 conditions. Carbon derived from EA thus mainly entered central metabolism through the TCA cycle.

280 Regarding N metabolism, the isotopic model confirmed the ammonium overflow predicted by the
281 GSM, with an ammonium production rate of 0.9 ± 0.2 mmol.g_{DW}^{-1}.h^{-1} (Fig.5C; Table S5; 12% of the N
282 from EA). This value is slightly lower than the optimal FBA-predicted value (3.0 mmol.g_{DW}^{-1}.h^{-1}, Fig.S7),
283 possibly because of an underestimation of the quantity of N required to form biomass (which was
284 determined during growth on glucose and ammonia as sole C and N sources, respectively[43]).

285 These isotope labelling experiments thus confirm the main predictions of the GSM, namely that EA can
286 be used as a C source for growth and that N overflow occurs under these conditions.

287 **Discussion**

288 The presence of functional Eut BMCs in *E. coli* has been suggested but never clearly demonstrated.
289 Focusing on the non-pathogenic laboratory strain *E. coli* K-12, our interdisciplinary results provide deep
290 molecular and functional insights into this native Eut BMC system and its importance for EA utilization.

291 We were able to visualize *E. coli* Eut BMCs *in cellula* by TEM and even more clearly by cryoET. The Eut
292 BMCs produced by WT *E. coli* K-12 W3110 were mostly well formed with an electron-dense core
293 separated from the surrounding cytoplasm by a continuous shell layer. Dark particles, presumably Eut
294 enzymes, were present in the core. No array-like particle arrangements were observed, contrary to
295 what has been reported for carboxysomes[45–49], but similar to observations of the Pdu BMCs of
296 *Acetonema longum*[50]. While recent efforts have allowed the internal organisation of carboxysomes to
297 be mapped out, much less is known of metabolosomes. Working on isolated Eut BMCs would facilitate
298 downstream structural characterisation; however, our attempts to purify *E. coli* Eut BMCs using
299 protocols established for Pdu BMCs[51] or α-carboxysomes[52] failed (data not shown). Apparently, the
300 protein-protein interactions that allow Eut BMCs to assemble and/or persist *in vivo* do not withstand
301 extracellular conditions[53]. Similar difficulties have previously been reported in *S. enterica*[51] and to our
302 knowledge intact Eut BMCs have never been purified from any bacterial species so far, suggesting that
303 Eut BMCs are intrinsically less stable than Pdu BMCs or carboxysomes.

304 We used fluorescence microscopy to observe Eut BMCs *in vivo*. $EutC_{(1-20)}$-GFP formed discrete puncta
305 in M9 glycerol EA B12 only so upon *eut* induction, i.e. when all the other Eut components were present.

306 EutC$_{(1-20)}$-GFP was likely encapsulated inside the Eut BMC core under these conditions. Unlike
307 fluorescently-tagged carboxysomes, which align along the cell axis[48], the EutC$_{(1-20)}$-GFP puncta moved
308 freely around the cytoplasm. This sort of mobility has also been observed for SeEutC$_{1-19}$-EGFP
309 encapsulated in *S. enterica* Eut BMCs *in vivo*[21,32]. Eut BMCs may interact with bacterial cytoskeleton
310 through shell-coating proteins, somewhat like Pdu BMCs do with PduV[54]. EutP and PduV share some
311 sequence homology (e.g. 28% primary structure identity and 54% similarity between EutP from *E. coli*
312 K-12 and PduV from *S. enterica* LT2), both containing a RAS-like GTPase superfamily domain
313 (Pfam10662). EutP may hence play a role in positioning the Eut BMCs, but this hypothesis remains to
314 validate experimentally. How Eut BMCs subcellular dynamics affect their metabolic functioning or
315 inheritance by daughter cells remains unclear. An EutK-mCherry fusion has recently been used to
316 visualize *Listeria monocytogenes* Eut BMCs *in vivo*[55], which appeared as immobile red puncta. Future
317 work should include the colocalization of core (e.g. EutC) and shell (e.g. EutK) elements to further
318 validate the location of the fluorescent reporters.

319 How many Eut BMCs do the *E. coli* K-12 W3110 cells contain under our culturing conditions and how
320 is the number of Eut BMCs regulated? Assuming that each GFP punctum corresponded to a single BMC,
321 our data indicate that there were 6 Eut BMCs per bacterium, but this count needs to be confirmed by
322 higher resolution approaches such as correlated light and electron microscopy[56]. In comparison,
323 around 3-4 GFP puncta per bacterium were observed in *S. enterica* after labelling Pdu BMCs with GFP[57].
324 TEM observations indicate that chemo-autotrophic bacteria contain 3 to 80 carboxysomes per cell[34,48].
325 The number of Eut BMCs likely depends on culture conditions[9]: resource availability and specific
326 regulatory networks (e.g. control by catabolic repression[10]) may modulate expression of the *eut*
327 operon. Even with 5 to 100 BMCs per *E. coli* W3110 WT, Eut BMCs would occupy just 0.2-4 % of the
328 total cytosolic volume.

329 This study also shows that the ability of *E. coli* K-12 to utilize EA as a N source hinges on the *eut* operon,
330 with minor reorganizations of the rest of the proteome. However, expressing *eut* from even a low copy
331 plasmid impaired growth. The underlying physiological cause is most likely the associated metabolic
332 burden because slower growth i) also occurred in a medium containing NH_4Cl as the N source
333 (indicating that the impairment is not simply due to impaired EA catabolism) and ii) was more
334 pronounced after inducing P_{trc} with IPTG. Overexpressing the *eut* operon increased the number of Eut
335 BMCs per bacterium observed by electron microscopy, up to several hundred under certain conditions
336 (e.g. LB IPTG). The same effect (i.e. more Eut BMCs and slower growth) has previously been observed
337 in *Enterococcus faecalis* upon suppressing a negative *eut* regulator[58]. As observed for other
338 proteins[59,60], fine-tuned regulation of the *eut* operon is necessary to achieve the desired metabolic
339 function at a manageable metabolic cost.

340 The protein complement of Eut BMCs remains unclear; however, our relative quantification of *E. coli*
341 Eut proteins *in vivo* can be used to make an educated guess. The most abundant candidate shell
342 component was hexameric (EutM), the second-most was trimeric (EutL) and the most dilute was
343 pentameric (EutN), reminiscent of the Pdu BMC system in *S. enterica*[61]. This is consistent with EutM
344 and EutL forming the facets and edges of the polyhedral shell together with other minor building blocks
345 (i.e. EutS and EutK)[17,62]. As a pentameric vertex protein[17,63], EutN is less abundant than the other shell
346 components. Among candidate core enzymes, the large (EutB) and small (EutC) subunits of EAL were
347 roughly equimolar, consistent with the holoenzyme's predicted oligomeric state $[(EutB_2EutC_2)_3]$[64].
348 NADH generating EutE acetaldehyde dehydrogenase was another major putative core component as
349 were Eut enzymes involved in cofactor recycling (EutG for NAD^+ and EutD for CoA-SH).

350 EutQ was found to be highly abundant, ten times more abundant than EutP, the other *eut*-encoded
351 acetate kinase[37]. We think that EutQ and EutP are localized outside the Eut BMC (i.e. on the shell

352 surface or soluble in the cytosol) so that any ATP generated upon EA-derived acetyl-P consumption
353 can feed into cellular metabolism. Moreover, EutP must be localized on the shell surface to interact
354 with cytoskeleton elements. However, our results do not allow any conclusions to be drawn about the
355 subcellular localizations of EutQ and EutP: either or both enzyme(s) could also be encapsulated within
356 BMCs *in vivo*. EutQ has been reported to interact with EutM *in vitro* and to facilitate the formation of
357 multiple Eut BMCs per bacterium[32]. Since ATP probably cannot transit through the pores in the shell[19],
358 any ATP produced in the core by EutQ and EutP when converting acetyl-P into acetate would have to
359 be recycled internally, e.g. to reactivate EAL after it undergoes catalytic inactivation[65,66]. During the
360 finalization of the present manuscript, a study was released showing the cytosolic localization of EutP
361 and the encapsulation of EutQ within Eut BMCs in *S. enterica* LT2 [67]. EutQ moreover seems to play a
362 central role in connecting the Eut BMC core and shell elements[67].

363 To our knowledge, the flux map reported here is the first to connect the Eut BMC with central
364 metabolism *in cellula*. Our results indicate that *E. coli* Eut BMCs leak non-negligible amounts of
365 acetaldehyde (up to 33 % of the C from EA). In comparison, about 13 and 28 % of the C from 1,2-PD
366 was found to be lost as propionaldehyde by the Pdu BMCs of *Salmonella enterica* [68] and *Propionobacter*
367 *freudenreichii*[69], respectively. Leakage may thus be a common feature of metabolosomes. However,
368 our cultures were performed under aerobic conditions with shaking, which favours gas exchanges and
369 acetaldehyde evaporation[20]. These conditions are different from those encountered within the gut
370 environment, where only limited quantities of oxygen diffuse through the mucosal surface to be
371 consumed by facultative anaerobes such as *E. coli*[70]. Hence, less acetaldehyde losses may occur *in vivo*
372 within the mammalian host. We did not observe any deleterious effect of acetaldehyde leakage on
373 growth, suggesting that the concentration of acetaldehyde remained below the toxicity threshold in
374 the cytosol[20]. In our model, the remaining acetaldehyde is converted inside the BMC core into
375 equimolar quantities of ethanol and acetyl-P before diffusing out through shell pores. Some of the EA-
376 derived C then enters central metabolism, mainly through the TCA cycle, to fuel growth. This result is
377 in line with a recent report demonstrating that *E. coli* assimilates acetate (here derived from
378 ethanolamine) with glycolytic substrates when the glycolytic flux is low, such as on glycerol[71], to feed
379 anabolism. But why then is *E. coli* K-12 W3110 WT unable to grow with EA as sole C source? Perhaps
380 the flux of EA assimilation simply did not meet cellular housekeeping demands. Additional comparisons
381 with other *E. coli* strains, including some capable of utilizing EA as sole C source[10,12], are required to
382 identify the underlying mechanisms.

383 Could some ancillary EUT1 proteins play a role in EA utilization? We detected 7 out of the 11 ancillary
384 EUT1 proteins by proteomics (TktB, TalA, MaeB, AmiA, YpeA, YfeY and YfeX), none of them being
385 differentially accumulated in M9 glycerol EA B12 VS M9 glycerol NH_4Cl. YpeA and YfeY have no known
386 biological functions. AmiA participates in septum formation during cell division[72]. YfeX is a peroxidase
387 that acts onto porphyrinogens to convert them into porphyrins [73]; *yfeX* is upregulated under anaerobic
388 conditions and may participate in respiratory complexes recycling. The contributions of AmiA and YfeX
389 to EA catabolism, if any, appears unclear. Under certain conditions, MaeB, TktB and TalA, on the other
390 hand, may funnel some EA-derived C through gluconeogenesis and the pentose phosphate pathway.
391 Malic enzyme activity plays an important metabolic role by connecting the TCA cycle with
392 gluconeogenesis[74]. The *maeB* expression is moreover induced when *E. coli* grows on acetate[75]. MaeB
393 may thus be key when *E. coli* grows using the EA-derived acetyl-P (or acetate) as its sole C source: after
394 conversion into acetyl-CoA, these EA-derived compounds first enter central metabolism through the
395 TCA cycle/glyoxylate shunt. MaeB would then direct some EA-derived C towards gluconeogenesis. TktB
396 and TalA both participate in the pentose phosphate pathway (PPP)[76]. TktB and TalA would next direct
397 some of the EA-derived C through the PPP, allowing the generation of multiple metabolites that are
398 essential for biomass formation (erythrose-4P, ribulose-5P…). TalA, like other aldolases[77], may also be

399 able to condensate some EA-derived acetaldehyde (leaking from the Eut BMCs) with glyceraldehyde-
400 3P to produce 1-deoxy-D-xylulose 5-phosphate (DXP), a precursor for the synthesis of vitamin B6. The
401 ancillary EUT1 proteins may hence funnel some EA-derived C for the accumulation of biomass.
402 However, in the present study, we had to perform our experiments in M9 glycerol EA B12 since *E. coli*
403 K-12 W3110 does not grow on M9 EA B12 (i.e. with EA as the sole C/N source). In our medium, glycerol
404 provides most C for both glycolysis and the pentose phosphate, as confirmed by the labelling patterns
405 of proteinogenic amino-acids. The ancillary EUT1 proteins implication should therefore be re-assessed
406 in *E. coli* strains that grow using EA as their C and N source, under more physiologically relevant
407 conditions.

408 By integrating our microscopy and fluxomics data, we calculated the mean EA conversion flux through
409 an individual *E. coli* K-12 Eut BMC *in cellula* (calculations in Supplementary Data 3): the value is close
410 to 0.300 fmol.BMC^{-1}.h^{-1} (or 0.600 fmol C.BMC^{-1}.h^{-1}). This is very close to the mean flux of 1,2-PD
411 conversion through an individual *S. enterica* Pdu BMC *in cellula* (0.350 fmol.BMC^{-1}.h^{-1}, or 1.050 fmol
412 C.BMC^{-1}.h^{-1}) calculated from previous experimental and modelling data[68,78]. The carboxylation rate
413 through an individual carboxysome varies from 0.03 to 4.82 fmol C.BMC^{-1}.h^{-1} depending on
414 conditions[79]. These BMC types seem to operate at similar overall turnover rates, despite having
415 different enzymatic core contents. Although they occupy an almost negligible fraction of the cytosolic
416 volume, our model predicts that Eut BMCs act as efficient nanobioreactors with total C fluxes
417 comparable to those of other major cellular metabolic processes (e.g. a glycolytic flux of 0.72 fmol.cell^{-}
418 ^{1}.h^{-1} or 2.16 fmolC.cell^{-1}.h^{-1} here).

419 Finally, we also found that EA served as a N source, with strong modifications in the levels of proteins
420 involved in nitrogen metabolism. The ammonium generated by EA catabolism was mostly used for
421 biomass production but the rest was excreted. The N:C molar ratio of EA (1:2) is higher than in the
422 elemental composition of *E. coli* (1:4)[80], which explains why our cultures acted as net ammonium
423 producers. Moreover, given that glycerol was the primary C source in M9 glycerol EA B12, the
424 proportion of excreted ammonium would likely be higher in other media with less organic C (e.g. M9
425 EA). Another study, released during the finalization of the present manuscript, showed that *E. coli*
426 Nissle 1917 also displays an ammonium overflow when grown on M9 EA B12 while *S. enterica* does
427 not[81]. This may have important physiological implications in the gut microbiome environment. Do EA-
428 utilizing bacteria release ammonium in the gut, making it available for surrounding micro-organisms?
429 EA utilization may influence the composition of complex bacterial communities through C and N
430 overflows.

431 **Conclusion**

432 The native *E. coli* Eut BMC has so far been overlooked by recent efforts to explore the natural diversity
433 of BMC structures and functions. Our interdisciplinary approach shows that the laboratory strain *E. coli*
434 K-12 W3110 produces well-formed Eut BMCs. These Eut BMCs act as orthogonal modules in the
435 cytosol, turning EA into usable N and C substrates for biomass formation, but with significant metabolic
436 overflow. However, some questions remain unanswered as to how the Eut BMCs operate, particularly
437 regarding the subcellular localization of certain Eut proteins (e.g. EutQ) and of cofactor recycling (e.g.
438 ATP). Several ancillary EUT1 proteins may be important for EA utilization but the hypothesis still awaits
439 direct experimental validation. The existence of a native subcellular compartmentalization system
440 shows that *E. coli* has a more complex metabolic organization than originally perceived.

441 **Materials and Methods**

442 Bacterial strains and culture conditions

443 *Media preparation*

444 Cloning experiments were performed in Lysogeny Broth (LB). For the physiological characterizations,
445 a nitrogen-free M9-medium was first assembled containing (final concentration in the medium): 17.4
446 $g \cdot L^{-1}$ $Na_2HPO_4 \cdot 12H_2O$, 3.03 $g \cdot L^{-1}$ KH_2PO4, 0.51 $g \cdot L^{-1}$ NaCl, 0.49 $g \cdot L^{-1}$ MgSO4 and 4.38 $mg \cdot L^{-1}$ $CaCl_2$.
447 Thiamine hydrochloride (100 $mg \cdot L^{-1}$) was also included, as well as 0.1 % (v/v) of a trace element
448 solution (final concentration in the medium: 15 $mg \cdot L^{-1}$ $Na_2EDTA \cdot 2H_2O$,4.5 $mg \cdot L^{-1}$ $ZnSO_4 \cdot 7H_2O$, 0.3
449 $mg \cdot L^{-1}$ $CoCl_2 \cdot 6H_2O$, 1 $mg \cdot L^{-1}$ $MnCl_2 \cdot 4H_2O$, 1 mg $\cdot L^{-1}$ H_3BO_3, 0.4 $mg \cdot L^{-1}$ $Na_2MoO \cdot 2H_2O$, 3 $mg \cdot L^{-1}$ FeSO4
450 $\cdot 7H_2O$, and 0.3 $mg \cdot L^{-1}$ $CuSO_4 \cdot 5H_2O$). In M9 glycerol ammonium, NH_4Cl (1.07 $g \cdot L^{-1}$ or 20 mM) was added
451 as the nitrogen source and glycerol (2.76 $g \cdot L^{-1}$ or 30 mM) as the organic carbon source. In M9 glycerol
452 EA B12, glycerol was the main organic carbon source (2.76 $g \cdot L^{-1}$ or 30 mM), ethanolamine was added
453 as the nitrogen source (1.22 $g \cdot L^{-1}$ or 20 mM; from a stock solution at 122 $g \cdot L^{-1}$ adjusted to pH 7 with
454 HCl 12 N) and cyanocobalamin was systematically included (200 nM). All media components were
455 autoclaved except for thiamine hydrochloride, the trace element solution, NH_4Cl and ethanolamine
456 that were filter-sterilized instead (Minisart 0.2 mm syringe filter, Sartorius, Germany). Antibiotics were
457 added to both solid and liquid media according to each strain's resistance profile [Ampicillin (Amp) at
458 100 $\mu g.mL^{-1}$, Kanamycin (Km) at 50 $\mu g.mL^{-1}$, Spectinomycin (Sp) at 50 $\mu g.mL^{-1}$ and/or Gentamycin (Gm)
459 at 10 $\mu g.mL^{-1}$]. Isopropyl-b-D-thiogalactoside (IPTG) (final concentration 20 µM) or
460 anhydrotetracycline (aTc) (final concentration 8ng mL^{-1} or 80 ng mL^{-1}) was also incorporated when
461 indicated. All chemical products were purchased from Sigma-Aldrich (France) unless otherwise
462 specified.

463 *Strains cultivation*

464 *E. coli* K-12 W3110 wild-type (WT) as well as several mutant derivatives were used (Table 1). All the
465 strains were cryopreserved at -80°C in LB with 25 % (w/v) glycerol. The strains were streaked onto LB
466 agar plates and incubated at 37°C for 16 h. An isolated single colony then served to inoculate 2 ml of
467 LB medium before culturing for 8h at 37°C under 200 rpm orbital shaking (Inova 4230, Brunswick
468 Scientific, United States). The optical density at 600 nm (OD_{600nm}) was measured with a Genesys 6
469 spectrophotometer (Thermo Fisher Scientific, United States). The preculture was next diluted into a
470 baffled shake flask (250 ml) containing 50 ml of modified M9-medium, aiming for a starting OD_{600nm} of
471 0.07.

472 After 16h of incubation at 37°C under 200 rpm shaking, the bacteria were collected by centrifugation
473 (4000 × g at room temperature for 3 min) and washed once using modified M9 medium. Finally, the
474 bacteria were inoculated into a baffled flask (250 mL) containing 50 ml of modified M9 medium, again
475 at a starting OD_{600nm} of 0.07. Cultures were performed at 37°C under 200 rpm shaking to proceed with
476 the physiological characterization. The following equation was employed to convert OD_{600nm} values
477 into corresponding biomass dry weight: $g_{DW} = 0.37 \times OD_{600nm}$.

478 When mentioned, cultures were made in a plate format instead. In this case, transparent flat-bottom
479 96 well plates (Sarstedt, Germany) covered with lids and containing 100 µl medium per well were used.
480 The culturing scheme was similar to that described for shake flasks. A CLARIOStar Plus (BMG LabTech,
481 Germany) plate reader apparatus allowed maintaining the cultures at 37°C under 200 rpm double
482 orbital shaking. Absorbance at 600 nm was measured every 10 min to estimate growth. Results were
483 analysed with the MARS Data Analysis software (BMG LabTech, Germany).

484 <u>Molecular biology</u>

485 *Cloning procedures*

486 Polymerase chain reactions (PCRs) for cloning purposes were performed using the high fidelity Phusion
487 DNA Polymerase (NEB, France). PCR products were purified with the NucleoSpin PCR Clean Up kit
488 (Macherey Nagel, Germany), quantified with a NanoDrop 2000 Spectrophotometer (Thermo Fisher
489 Scientific, France) and assembled by In-Fusion (TaKaRa, Japan). After purification with the NucleoSpin
490 Plasmid kit (Macherey Nagel, Germany), the generated plasmids were verified by Sanger Sequencing.

491 *CRISPR-Cas9 genome editing*

492 The system described by Jiang and coworkers was utilized in this study[27]. To generate the Δ*eut* strain,
493 a pTargetF plasmid for *eutG* (pTargetF_eutG) was first constructed. The linear backbone from pTargetF
494 was amplified with primers F_bb1/R_bb1 (see Table S1 for primer sequences). The *eutG* targeting
495 protospacer (PAM shown in bold: CGGCACACCTTCGGTCAATG**CGG**) was amplified with primers
496 F_eutGgRNA/R_eutGgRNA. The generated amplicons were then assembled by In-Fusion to generate
497 pTarget_eutG (Sp^R). Next, the 500 nt situated directly upstream of the P*eut* promoter (upper homology
498 arm) were amplified from purified *E. coli* K-12 W3110 WT gDNA with F_UA1/R_UA1. The same was
499 achieved for the 500 nt downstream of *eutR* (lower homology arm) with F_LA1/R_LA1. The backbone
500 from pUC19 was amplified with F_bb2/R_bb2 and all three fragments were assembled by In-Fusion to
501 yield pHD_Δeut (Amp^R). The linear fragment containing both homology arms was amplified from
502 pHD_Δeut using F_HD1/R_HD1. pTarget_eutG as well as the produced linear fragment were finally
503 electroporated into pCas-containing *E. coli* K-12 W3110 WT bacteria to obtain chromosomally edited
504 Δ*eut* strains. After genotyping, the edited mutants were cured of pTarget_eutG and pCas as described
505 previously.

506 The *SS9* targeting protospacer (TCTGGCGCAGTTGATATGTA**AGG**) was cloned by In-Fusion into pTargetF
507 using primers F_SS9gRNA/R_SS9gRNA and F_bb1/R_bb1, yielding pTargetF_SS9. The 1000 nt upstream
508 of *SS9* were amplified from purified *E. coli* K-12 W3110 WT gDNA with F_UA2/R_UA2, including
509 mutations to suppress the above-mentioned PAM (i.e. AGG to CAA), the 1000 nt downstream of *SS9*
510 with F_LA2/R_LA2. The EutC-GFP and $EutC_{1-20}$-GFP encoding cassettes ($P_{LtetO-1}$ promoter, T_{LT0}
511 terminator) were synthesized and cloned with flanking the SS9 homology arms into pUC19, yielding
512 pHD_SS9_eutC-GFP and pHD_SS9_$eutC_{1-20}$-GFP.

513 *Assembly of pEut_WT.*

514 The linear backbone from pSEVA661_Ptrc (modified version of pSEVA661 bearing a *lacI*^{q} expression
515 cassette and the P_{trc} promoter cloned in its MCS) was amplified with primers F_bb3/R_bb3 (see Table
516 S1). The complete *eut* operon was amplified from isolated *E. coli* K-12 W3110 WT gDNA using
517 F_eut1/R_eut1, F_eut2/R_eut2 as well as F_eut3/R_eut3. The generated amplicons were assembled
518 by In-Fusion to produce the low copy plasmid pEut_WT (Gm^R). Next generation DNA sequencing on an
519 Ion S5 System (Thermo Fisher Scientific, France) was performed at the GeT_Biopuces platform (TBI,
520 INSA Toulouse, France) to verify that the plasmid was properly assembled.

521 Microscopy observations

522 *Epifluorescence microscopy*

523 Samples (equivalent to 0.6 µl culture at OD_{600nm} = 1) were collected after reaching stationary phase
524 and deposited onto GeneFrames (ThermoFisher) containing solidified C-/N-free M9 medium with 1 %
525 agarose. Phase contrast and fluorescence microscopy was performed at room temperature using an
526 automated inverted epifluorescence microscope (Nikon Ti-E/B) equipped with the "perfect focus
527 system" (PFS, Nikon), a phase contrast objective (Plan Apo 100x Oil Ph3 DM NA1.4), a Lumencor
528 SpectraX Light Engine as the illumination source (Ex: 475/34 for GFP), Semrock Brightline multiband

529 dichroic filters (FF409/493/573/652-Di02 for GFP), Semrock emission filters (Em: 536BP40 for GFP) and
530 a Flash4.0 sCMOS camera (Hamamatsu). Fluorescence images were captured and processed using Nis-
531 Elements AR software (Nikon) as well as Fiji[82]. To visualize the mobile fluorescent puncta, pictures were
532 taken every 5 sec over an interval of 30 sec. The puncta were counted manually within n = 30 bacterial
533 cells per samples.

534 *TEM visualization*

535 Samples (equivalent to 1 ml of culture at OD_{600nm} = 1) were collected upon reaching stationary phase
536 by centrifugation at 3000 × g for 3 minutes. Pellets were resuspended in fixation solution (2.5 %
537 glutaraldehyde, 0.1 M cacodylate pH 7.4 as well as 0,04 % w/v ruthenium red) and incubated for 16h
538 at 4°C. Samples were post-fixated in 1 % osmium tetroxide, dehydrated stepwise in ethanol and
539 eventually embedded in the Embed 812 resin (Electron Microscopy Sciences) with a Leica AMW
540 automated device. Thin sections (70 nm width) were stained (solution containing 3 % uranyl acetate
541 in 50 % ethanol as well as Reynold's lead citrate) and observed using a HT 7700 Hitachi transmission
542 electron microscope (accelerating voltage 80 kV, CCD AMT XR41 camera).

543 *cryoET visualization*

544 Samples (equivalent to 1 ml of culture at OD_{600nm} = 1) were collected upon reaching stationary phase
545 and centrifuged at 3000 × g for 3 minutes. Supernatants were discarded. Pellets were washed twice
546 in 1X PBS buffer pH 7.4 and finally resuspended in 50µl of 1X PBS 7.4.

547 Grid preparation: 3.4 µL of sample were deposited onto glow-discharged lacey carbon grids and placed
548 in the thermostatic chamber of a Leica EM-GP automatic plunge freezer, set at 20°C and 95 % humidity.
549 Excess solution was removed by blotting with Whatman n°1 filter paper for 2.5 seconds, and the grids
550 were immediately flash frozen in liquid ethane at -185°C.

551 Cryo-electron tomography: Tilt-series were acquired on a Talos Arctica (Thermo Fisher Scientific)
552 operated at 200 kV in parallel beam condition using either a K2 (for mutant cells) or K3 (for WT
553 condition) Summit direct electron detector and a BioQuantum energy filter (Gatan Inc.) operated in
554 zero-loss mode with a slit width of 20 eV. For WT cells, data collection was carried out using Tomo
555 software (Thermo Fisher Scientific), at a nominal magnification of x31,000 with a calibrated pixel size
556 of 2,78Å. For mutant cells, a nominal magnification of x49000 was used with a calibrated pixel size of
557 2.84Å. In both conditions, tilt series were acquired following the dose symmetric scheme[83] between
558 +50° and −50° with a 2° tilt increment and a defocus range between -10 and -12 µm. Each tilt image
559 was acquired in electron counting mode with cumulative electron dose of 140e-/A² fractionated into
560 ten frames.

561 Tomogram reconstruction and segmentation: Movie frames were aligned using MotionCor2[84] and tilt
562 series were mutually aligned by using 10nm gold particles as fiducial markers and the 3D volumes
563 (tomograms) were reconstructed with weighted back projection using IMOD v.4.11.16[85] software
564 packages with a binning factor of 4. Tomograms were finally denoised and contrast enhanced, boosting
565 the signal to noise ratio (SNR), using Topaz[86] and nonlinear anisotropic diffusion filtering, respectively.
566 Individual objects in tomograms are then segmented using EMAN2 TomoSeg[87], and surfaces of each
567 segmented object are generated and visualized in ChimeraX[88].

568 <u>Proteomics analysis</u>

569 *E. coli* K-12 W3110 WT cultures were grown at 37°C under 200 rpm orbital shaking, in 250 ml flasks
570 containing 50 ml M9 glycerol EA B12. Upon reaching OD_{600nm} = 1, samples (40 ml) were collected and
571 centrifuged 5 min at 4000 × g. Supernatant was discarded, pellet was resuspended in 3 ml Lysis Buffer

572 [100mM triethylammonium bicarbonate (TEAB) Buffer pH 8,5 with 2,5 % w/v SDS] at 4°C. Bacteria
573 were lyzed by sonication (Fisherbrand sonicator equipped with a microprobe: 20 % power, 20 sec on,
574 30 sec off, cycle repeated twice). After centrifugation 8 min at 13000 × g, supernatant was collected.
575 The protein concentration was determined using a BCA assay.

576 Dried protein extracts (40 µg) were solubilized with 25 µl of 5% SDS. Proteins were submitted to
577 reduction and alkylation of cysteine residues by addition of TCEP and chloroacetamide to a final
578 concentration respectively of 10 mM and 40 mM. Protein samples were then processed for trypsin
579 digestion on S-trap Micro devices (Protifi) according to manufacturer's protocol, with the following
580 modifications: precipitation was performed using 211 µl S-Trap buffer; 4 µg Trypsin was added per
581 sample for digestion, in 25 µl TEAB 50mM pH8.

582 Tryptic peptides were resuspended in 20 µl of 2% acetonitrile and 0.05% trifluoroacetic acid and
583 analyzed by nano-liquid chromatography (LC) coupled to tandem MS, using an UltiMate 3000 system
584 (NCS-3500RS Nano/Cap System; Thermo Fisher Scientific) coupled to an Orbitrap QExactive Plus mass
585 spectrometer (Thermo Fisher Scientific). 5 µl of each sample was loaded on a C18 precolumn (300 µm
586 inner diameter × 5 mm, Thermo Fisher Scientific) in a solvent made of 2% acetonitrile and 0.05%
587 trifluoroacetic acid, at a flow rate of 20 µl/min. After 5 min of desalting, the precolumn was switched
588 online with the analytical C18 column (75 µm inner diameter × 50 cm, in-house packed with Reprosil
589 C18) equilibrated in 95% solvent A (5% acetonitrile, 0.2% formic acid) and 5% solvent B (80%
590 acetonitrile, 0.2% formic acid). Peptides were eluted using a 5%-50% gradient of solvent B over 115
591 min at a flow rate of 300 nl/min. The mass spectrometer was operated in data-dependent acquisition
592 mode with the Xcalibur software. MS survey scans were acquired with a resolution of 70,000 and an
593 AGC target of 3e6. The 10 most intense ions were selected for fragmentation by high-energy collision
594 induced dissociation, and the resulting fragments were analyzed at a resolution of 17500, using an AGC
595 target of 1e5 and a maximum fill time of 50 ms. Dynamic exclusion was used within 30 s to prevent
596 repetitive selection of the same peptide.

597 Raw MS files were processed with the Mascot software (version 2.7.0) for database search and
598 Proline[89] for label-free quantitative analysis (version 2.1.2). Data were searched against *Escherichia coli*
599 entries of the UniProtKB protein database (release Swiss-Prot 2019_11_05, 23,135 entries).
600 Carbamidomethylation of cysteines was set as a fixed modification, whereas oxidation of methionine
601 was set as variable modifications. Specificity of trypsin/P digestion was set for cleavage after K or R,
602 and two missed trypsin cleavage sites were allowed. The mass tolerance was set to 10 ppm for the
603 precursor and to 20 mmu in tandem MS mode. Minimum peptide length was set to 7 amino acids, and
604 identification results were further validated in Proline by the target decoy approach using a reverse
605 database at both a PSM and protein false-discovery rate of 1%. For label-free relative quantification of
606 the proteins across biological replicates and conditions, cross-assignment of peptide ions peaks was
607 enabled inside group with a match time window of 1 min, after alignment of the runs with a tolerance
608 of +/- 600 s.

609 The mass spectrometry proteomics data have been deposited to the ProteomeXchange Consortium
610 via the PRIDE partner repository with the dataset identifier PXD048973.

611 Metabolomics analysis

612 *^{1}H-NMR analysis of culture supernatants*

613 *E. coli* K-12 W3110 WT cultures were grown at 37°C under 200 rpm orbital shaking, in 250 ml flasks
614 containing 50 ml M9 glycerol NH4Cl or EA. For the labelling experiment, fully-labelled ethanolamine
615 ($^{13}C_2$-ethanolamine, InnovaChem, France) was employed in the last culturing step for M9 glycerol EA

616 B12. Samples (500 µL) were collected every 60 min. Bacteria were immediately removed by filtration
617 (Minisart 0.2 mm syringe filter, Sartorius, Germany) and the flow-through was kept at -20°C until
618 further analysis. The flow-through was thawed and mixed (180 µL) with 20 µL of an internal standard
619 containing 2.35 g/l deuterated trimethylsilylpropanoic acid (TSP-d4) solubilized in D_2O. The ^{1}H-NMR
620 analyses were performed using a quantitative zgpr30 sequence with water pre-saturation prior to
621 acquisition on an Avance III 500-MHz spectrometer. The parameters were as follows: 286 K, 128K
622 points, 4 dummy scans, 64 scans, interscan delay of 8.98 s. Three biological replicates were included
623 for each medium. For the ammonium quantification experiment, the filtration flow through (690 µl,
624 diluted 4X in MQ H2O) was mixed with 7.3 µl 4M H_2SO_4 and 2.7 µl MQ H_2O[90]. TSP-d4 dissolved in D2O
625 (60 µl) was added to 540 µl of the mixture. A solvent suppression proton NMR sequence (zggpw5) at
626 286K with 32K points, 64 scans, 4 dummy scans, and an interscan delay of 10 s was then applied.
627 Quantification was achieved through an external NH_4Cl standard curve (200 mM, 8 mM, 2 mM, 0.5
628 mM and 0.1 mM NH_4Cl diluted in M9 glycerol) analysed with ^{1}H-NMR with the same acquisition
629 parameters and the same sample preparation. Quantification of ammonium in solution was achieved
630 by integration of NMR signals of protons (between 6.9 and 7.4 ppm) attached to nitrogen in an acidic
631 medium, according to the different occurring species (i.e. NH_4, NH_3D, NH_2D_2,) in a mixture of H_2O and
632 D_2O (NHD_3 and ND_4 in negligible amounts were not detected).

633 *Isotopic profiling of proteinogenic amino acids*

634 The same cultures as for NMR analyses were used. Biomass (500µl) was harvested at an OD_{600nm} of 1
635 corresponding to mid-exponential phase. The biomass sample was immediately mixed with 3,5 ml pre-
636 chilled (-20°C) quenching solution made of methanol-acetonitrile-H_2O (4:4:2) containing 125 mM
637 formic acid. The mixture was incubated at -20°C for at least 2 h and then centrifugated at 4500 × g
638 4°C for 5 min. The pellet was stored at -20°C until further usage. After thawing, the pellet was
639 evaporated to dryness with an Orbitrap apparatus (Thermo Fisher Scientific, USA) and hydrolyzed for
640 16h at 105°C with 500 µL HCl 6N. Samples were washed twice before being resuspended into 250 µL
641 ultrapure water and diluted (1:700) for the mass spectrometry analysis. LC-MS was performed on an
642 Ultimate 3000 HPLC system (Dionex, CA, USA) coupled to an LTQ Orbitrap Velos mass spectrometer
643 (Thermo Fisher Scientific, USA). Full scan HRMS analyses were performed in positive FTMS mode, the
644 acquisition parameters and data analysis pipeline being identical to that previously described by
645 Heuillet and coworkers[91]. IsoCor[92] allowed correcting for natural isotopic abundances to determine the
646 carbon isotopologue distributions (CIDs).

647 Modelling

648 *Extracellular uptake and production fluxes*

649 Glycerol and ethanolamine uptake fluxes, acetate and ethanol production fluxes, and growth rates
650 were calculated from glycerol, ethanolamine, acetate, ethanol, and biomass concentration−time
651 profiles using PhysioFit (v1.0.1[41], https://github.com/MetaSys-LISBP/PhysioFit). Ethanol evaporation
652 was considered when calculating ethanol production flux, as detailed in Peiro et al.[93] using an
653 evaporation constant of 0.0379 h^{-1} that was determined experimentally.

654 *Genome-scale modelling of glycerol and ethanolamine co-metabolism.*

655 The iML1515 *E. coli* genome scale model[43] was first updated by incorporating the EA assimilation
656 reactions catalysed by Eut enzymes (EutBC, EutG, EutE, EutD as well as EutQ/P) and the Eut BMC
657 subcellular compartment. We assumed that EutBC, EutG, EutE and EutD were all encapsulated within
658 the Eut BMC core as suggested previously[20], while EutQ/P were assumed to be cytosolic. We also
659 assumed cofactors (i.e. NAD(H) and CoA-SH) to not exchange between the eut BMC and the cytosol,

660 thus being recycled internally within the Eut BMC core. We finally assumed that acetate and ethanol
661 originated from the Eut BMCs. Flux balance analyses and flux variability analyses were carried out using
662 *cobrapy*[94] after constraining exchange fluxes with experimental uptake fluxes of *E. coli* K-12 W3110 WT
663 (see results). The final model iDJ1518 and the scripts used to perform the calculations can be found at
664 https://github.com/MetaSys-LISBP/ethanolamine_metabolism. The genome-scale model is also
665 available from the BioModels database[95] (http://www.ebi.ac.uk/biomodels) with identifier
666 MODEL2403010003.

667 *^{13}C-metabolic flux analysis.*

668 To quantify intracellular fluxes during growth of *E. coli* on glycerol and ethanolamine, we constructed
669 a dynamic ^{13}C-flux model following the approach detailed before[96] . The model contains 21 reactions,
670 20 species, and 3 compartments (the environment, the cytoplasm and the eut BMCs), and represents
671 five processes: i) growth, ii) glycerol uptake and conversion into acetyl-phosphate (AcP) by glycolysis,
672 iii) ethanolamine assimilation and conversion through the eut BMCs, iv) AcP utilization by the TCA
673 cycle, v) acetate, acetaldehyde, ethanol and ammonia excretion (Figure 5).

674 The differential equations, which balance the concentrations of extracellular compounds (biomass,
675 glycerol, ethanolamine, acetate and ethanol) and intracellular compounds (AcP, AcCoA, ethanolamine,
676 ethanol, acetate, glycerol, NAD(H) and ammonia), were completed with isotopic equations for
677 parameter estimation. As detailed before[97], we considered all reactions (except biomass synthesis)
678 separately for unlabeled and labelled reactants. Fluxes were assumed to be constant over time since
679 the cells were assumed to be at metabolic steady-state during exponential growth phase. We also took
680 ethanol evaporation into account, which was modeled with a mass action rate law, using the
681 evaporation constant determined experimentally in this study. The final model has 13 free parameters
682 in total. These parameters (p) were estimated by fitting to the experimentally determined
683 concentration dynamics of biomass, glycerol, ethanolamine, ethanol and unlabeled and labelled
684 acetate, by minimizing the objective function f defined as the weighted sum of squared errors:

685 $f(p) = \sum_i \left(\frac{x_i - y_i(p)}{\sigma_i}\right)^2$ where x_i is the experimental value of data point i, with an experimental
686 standard deviation σ_i, and $y_i(p)$ is the corresponding simulated value. The objective function f was
687 minimised using the particle swarm optimisation algorithm (2,000 iterations with a swarm size of 50).
688 The experimental and fitted data of one biological replicate are shown in Figure 5, and detailed results
689 for all replicates are provided in Supplementary Figure 7 and Supplementary Data 2.

690 The model was constructed and analysed using COPASI[98] (v4.27) and is provided in SBML and COPASI
691 formats in the Supplementary data 2 and at https://github.com/MetaSys-
692 LISBP/ethanolamine_metabolism. The model has also been deposited in the Biomodels database
693 (https://www.ebi.ac.uk/biomodels)[95] with the identifier MODEL2403010002 to ensure reproducibility
694 and reusability. Extensive details on the model are provided in Supplementary Data 2.

695 *Calculation of the flux through individual BMCs*

696 All the detailed calculations are given in Supplementary Data 3.

697 **Acknowledgements:**

698 We thank Isabelle Fourquaux (CMEAB) and Sylvain Cantaloube (CBI-LITC) for their technical help. This
699 work was funded by grants from INRAE (NANOBEs and ColiMATTERS projects) and by the ANR
700 (FUNCEMM, ANR-23-CE44-0038). The work was also funded in part by grants from the Région
701 Occitanie, European funds (Fonds Européens de Développement Régional, FEDER), Toulouse

Métropole, and the French Ministry of Research with the Investissement d'Avenir Infrastructures Nationales en Biologie et Santé program (ProFI, Proteomics French Infrastructure project, ANR-10-INBS-08). We acknowledge the METi imaging facility, member of the national infrastructure France-BioImaging supported by the French National Research Agency (ANR-10-INBS-04).

Bibliography:

1. Shively, J. M., Decker, G. L. & Greenawalt, J. W. Comparative ultrastructure of the thiobacilli. *J. Bacteriol.* **101**, 618–627 (1970).

2. Chen, P., Andersson, D. I. & Roth, J. R. The control region of the pdu/cob regulon in Salmonella typhimurium. *J. Bacteriol.* **176**, 5474–5482 (1994).

3. Kofoid, E., Rappleye, C., Stojiljkovic, I. & Roth, J. The 17-gene ethanolamine (eut) operon of Salmonella typhimurium encodes five homologues of carboxysome shell proteins. *J. Bacteriol.* **181**, 5317–5329 (1999).

4. Sutter, M., Melnicki, M. R., Schulz, F., Woyke, T. & Kerfeld, C. A. A catalog of the diversity and ubiquity of bacterial microcompartments. *Nat. Commun.* **12**, 1–12 (2021).

5. Stojiljkovic, I., Bäumler, A. J. & Heffron, F. Ethanolamine utilization in Salmonella typhimurium: nucleotide sequence, protein expression, and mutational analysis of the cchA cchB eutE eutJ eutG eutH gene cluster. *J. Bacteriol.* **177**, 1357–1366 (1995).

6. Bertin, Y. *et al.* Enterohaemorrhagic Escherichia coli gains a competitive advantage by using ethanolamine as a nitrogen source in the bovine intestinal content. *Environ. Microbiol.* **13**, 365–377 (2011).

7. Kaval, K. G. & Garsin, D. A. Ethanolamine utilization in bacteria. *MBio* **9**, (2018).

8. Zepeda-Rivera, M. *et al.* A distinct Fusobacterium nucleatum clade dominates the colorectal cancer niche. *Nature* **628**, 424–432 (2024).

9. Dadswell, K. *et al.* Bacterial microcompartment-mediated ethanolamine metabolism in Escherichia coli urinary tract infection. *Infect. Immun.* **87**, e00211-19 (2019).

10. Jones, P. W. & Turner, J. M. Interrelationships between the enzymes of ethanolamine metabolism in Escherichia coli. *Microbiology* **130**, 299–308 (1984).

11. Rowley, C. A., Anderson, C. J. & Kendall, M. M. Ethanolamine influences human commensal Escherichia coli growth, gene expression, and competition with enterohemorrhagic E. coli O157: H7. *MBio* **9**, e01429-18 (2018).

12. de Gouveia, M. I. M., Daniel, J., Garrivier, A., Bernalier-Donadille, A. & Jubelin, G. Diversity of ethanolamine utilization by human commensal Escherichia coli. *Res. Microbiol.* **174**, 103989 (2023).

13. Kendall, M. M., Gruber, C. C., Parker, C. T. & Sperandio, V. Ethanolamine controls expression of genes encoding components involved in interkingdom signaling and virulence in enterohemorrhagic Escherichia coli O157: H7. *MBio* **3**, e00050-12 (2012).

14. Tsoy, O., Ravcheev, D. & Mushegian, A. Comparative genomics of ethanolamine utilization. *J. Bacteriol.* **191**, 7157–7164 (2009).

15. Stewart, K. L., Stewart, A. M. & Bobik, T. A. Prokaryotic organelles: bacterial microcompartments in E. coli and Salmonella. *EcoSal Plus* **9**, (2020).

743 16. Axen, S. D., Erbilgin, O. & Kerfeld, C. A. A taxonomy of bacterial microcompartment loci
744 constructed by a novel scoring method. *PLoS Comput Biol* **10**, e1003898 (2014).

745 17. Sutter, M., Greber, B., Aussignargues, C. & Kerfeld, C. A. Assembly principles and structure of
746 a 6.5-MDa bacterial microcompartment shell. *Science (80-.).* **356**, 1293–1297 (2017).

747 18. Tanaka, S., Sawaya, M. R. & Yeates, T. O. Structure and mechanisms of a protein-based
748 organelle in Escherichia coli. *Science (80-.).* **327**, 81–84 (2010).

749 19. Huseby, D. L. & Roth, J. R. Evidence that a metabolic microcompartment contains and recycles
750 private cofactor pools. *J. Bacteriol.* **195**, 2864–2879 (2013).

751 20. Penrod, J. T. & Roth, J. R. Conserving a volatile metabolite: a role for carboxysome-like
752 organelles in Salmonella enterica. *J. Bacteriol.* **188**, 2865–2874 (2006).

753 21. Choudhary, S., Quin, M. B., Sanders, M. A., Johnson, E. T. & Schmidt-Dannert, C. Engineered
754 protein nano-compartments for targeted enzyme localization. *PLoS One* **7**, e33342 (2012).

755 22. Aussignargues, C., Paasch, B. C., Gonzalez-Esquer, R., Erbilgin, O. & Kerfeld, C. A. Bacterial
756 microcompartment assembly: The key role of encapsulation peptides. *Commun. Integr. Biol.*
757 **8**, e1039755 (2015).

758 23. Shively, J. M. *et al.* Sequence homologs of the carboxysomal polypeptide CsoS1 of the
759 thiobacilli are present in cyanobacteria and enteric bacteria that form carboxysomes-
760 polyhedral bodies. *Can. J. Bot.* **76**, 906–916 (1998).

761 24. Brinsmade, S. R., Paldon, T. & Escalante-Semerena, J. C. Minimal functions and physiological
762 conditions required for growth of Salmonella enterica on ethanolamine in the absence of the
763 metabolosome. *J. Bacteriol.* **187**, 8039–8046 (2005).

764 25. Chessher, A., Breitling, R. & Takano, E. Bacterial microcompartments: biomaterials for
765 synthetic biology-based compartmentalization strategies. *ACS Biomater. Sci. Eng.* **1**, 345–351
766 (2015).

767 26. Held, M., Quin, M. B. & Schmidt-Dannert, C. Eut bacterial microcompartments: insights into
768 their function, structure, and bioengineering applications. *Microb. Physiol.* **23**, 308–320
769 (2013).

770 27. Jiang, Y. *et al.* Multigene editing in the Escherichia coli genome via the CRISPR-Cas9 system.
771 *Appl. Environ. Microbiol.* **81**, 2506–2514 (2015).

772 28. Amann, E., Ochs, B. & Abel, K.-J. Tightly regulated tac promoter vectors useful for the
773 expression of unfused and fused proteins in Escherichia coli. *Gene* **69**, 301–315 (1988).

774 29. Silva-Rocha, R. *et al.* The Standard European Vector Architecture (SEVA): a coherent platform
775 for the analysis and deployment of complex prokaryotic phenotypes. *Nucleic Acids Res.* **41**,
776 D666–D675 (2013).

777 30. Bassalo, M. C. *et al.* Rapid and efficient one-step metabolic pathway integration in E. coli. *ACS*
778 *Synth. Biol.* **5**, 561–568 (2016).

779 31. Lutz, R. & Bujard, H. Independent and tight regulation of transcriptional units in Escherichia
780 coli via the LacR/O, the TetR/O and AraC/I1-I2 regulatory elements. *Nucleic Acids Res.* **25**,
781 1203–1210 (1997).

782 32. Held, M. *et al.* Engineering formation of multiple recombinant Eut protein nanocompartments
783 in E. coli. *Sci. Rep.* **6**, 24359 (2016).

784 33. Lee, M. J., Palmer, D. J. & Warren, M. J. Biotechnological advances in bacterial

785 microcompartment technology. *Trends Biotechnol.* **37**, 325–336 (2019).

786 34. Iancu, C. V *et al.* Organization, structure, and assembly of α-carboxysomes determined by
787 electron cryotomography of intact cells. *J. Mol. Biol.* **396**, 105–117 (2010).

788 35. Szklarczyk, D. *et al.* STRING v11: protein–protein association networks with increased
789 coverage, supporting functional discovery in genome-wide experimental datasets. *Nucleic*
790 *Acids Res.* **47**, D607–D613 (2019).

791 36. Schwanhäusser, B. *et al.* Global quantification of mammalian gene expression control. *Nature*
792 **473**, 337–342 (2011).

793 37. Moore, T. C. & Escalante-Semerena, J. C. The EutQ and EutP proteins are novel acetate
794 kinases involved in ethanolamine catabolism: physiological implications for the function of the
795 ethanolamine metabolosome in S almonella enterica. *Mol. Microbiol.* **99**, 497–511 (2016).

796 38. Javelle, A., Severi, E., Thornton, J. & Merrick, M. Ammonium sensing in Escherichia coli: role of
797 the ammonium transporter AmtB and AmtB-GlnK complex formation. *J. Biol. Chem.* **279**,
798 8530–8538 (2004).

799 39. van Heeswijk, W. C., Westerhoff, H. V & Boogerd, F. C. Nitrogen assimilation in Escherichia
800 coli: putting molecular data into a systems perspective. *Microbiol. Mol. Biol. Rev.* **77**, 628–695
801 (2013).

802 40. Weissbach, H. & Brot, N. Regulation of methionine synthesis in Escherichia coli. *Mol.*
803 *Microbiol.* **5**, 1593–1597 (1991).

804 41. Le Gregam, L. *et al.* PhysioFit: a software to quantify cell growth parameters and extracellular
805 fluxes. *bioRxiv* 2010–2023 (2023).

806 42. Orth, J. D., Thiele, I. & Palsson, B. Ø. What is flux balance analysis? *Nat. Biotechnol.* **28**, 245–
807 248 (2010).

808 43. Monk, J. M. *et al.* i ML1515, a knowledgebase that computes Escherichia coli traits. *Nat.*
809 *Biotechnol.* **35**, 904–908 (2017).

810 44. Schuetz, R., Kuepfer, L. & Sauer, U. Systematic evaluation of objective functions for predicting
811 intracellular fluxes in Escherichia coli. *Mol. Syst. Biol.* **3**, 119 (2007).

812 45. Cameron, J. C., Wilson, S. C., Bernstein, S. L. & Kerfeld, C. A. Biogenesis of a bacterial
813 organelle: the carboxysome assembly pathway. *Cell* **155**, 1131–1140 (2013).

814 46. Faulkner, M. *et al.* Direct characterization of the native structure and mechanics of
815 cyanobacterial carboxysomes. *Nanoscale* **9**, 10662–10673 (2017).

816 47. Ni, T. *et al.* Structure and assembly of cargo Rubisco in two native α-carboxysomes. *Nat.*
817 *Commun.* **13**, 4299 (2022).

818 48. Savage, D. F., Afonso, B., Chen, A. H. & Silver, P. A. Spatially ordered dynamics of the bacterial
819 carbon fixation machinery. *Science (80-.).* **327**, 1258–1261 (2010).

820 49. Evans, S. L. *et al.* Single-particle cryo-EM analysis of the shell architecture and internal
821 organization of an intact α-carboxysome. *Structure* **31**, 677–688 (2023).

822 50. Tocheva, E. I. *et al.* Structure and expression of propanediol utilization microcompartments in
823 Acetonema longum. *J. Bacteriol.* **196**, 1651–1658 (2014).

824 51. Sturms, R., Streauslin, N. A., Cheng, S. & Bobik, T. A. In Salmonella enterica, ethanolamine
825 utilization is repressed by 1, 2-propanediol to prevent detrimental mixing of components of

826 two different bacterial microcompartments. *J. Bacteriol.* **197**, 2412–2421 (2015).

827 52. Fang, Y. *et al.* Engineering and modulating functional cyanobacterial CO2-fixing organelles.
828 *Front. Plant Sci.* **9**, 739 (2018).

829 53. Tsai, S. J. & Yeates, T. O. Bacterial microcompartments: insights into the structure,
830 mechanism, and engineering applications. *Prog. Mol. Biol. Transl. Sci.* **103**, 1–20 (2011).

831 54. Parsons, J. B. *et al.* Synthesis of empty bacterial microcompartments, directed organelle
832 protein incorporation, and evidence of filament-associated organelle movement. *Mol. Cell* **38**,
833 305–315 (2010).

834 55. Chatterjee, A., Kaval, K. G. & Garsin, D. A. Role of Ethanolamine Utilization and Bacterial
835 Microcompartment Formation in Listeria monocytogenes Intracellular Infection. *bioRxiv*
836 2012–2023 (2023).

837 56. Hoffman, D. P. *et al.* Correlative three-dimensional super-resolution and block-face electron
838 microscopy of whole vitreously frozen cells. *Science (80-.).* **367**, eaaz5357 (2020).

839 57. Kennedy, N. W. *et al.* Linking the Salmonella enterica 1, 2-propanediol utilization bacterial
840 microcompartment shell to the enzymatic core via the shell protein PduB. *J. Bacteriol.* **204**,
841 e00576-21 (2022).

842 58. Kaval, K. G. *et al.* Ethanolamine utilization and bacterial microcompartment formation are
843 subject to carbon catabolite repression. *J. Bacteriol.* **201**, e00703-18 (2019).

844 59. Glick, B. R. Metabolic load and heterologous gene expression. *Biotechnol. Adv.* **13**, 247–261
845 (1995).

846 60. Ceroni, F. *et al.* Burden-driven feedback control of gene expression. *Nat. Methods* **15**, 387–
847 393 (2018).

848 61. Yang, M. *et al.* Decoding the stoichiometric composition and organisation of bacterial
849 metabolosomes. *Nat. Commun.* **11**, 1976 (2020).

850 62. Kalnins, G. *et al.* Encapsulation mechanisms and structural studies of GRM2 bacterial
851 microcompartment particles. *Nat. Commun.* **11**, 388 (2020).

852 63. Wheatley, N. M., Gidaniyan, S. D., Liu, Y., Cascio, D. & Yeates, T. O. Bacterial
853 microcompartment shells of diverse functional types possess pentameric vertex proteins.
854 *Protein Sci.* **22**, 660–665 (2013).

855 64. Shibata, N. *et al.* Crystal structures of ethanolamine ammonia-lyase complexed with
856 coenzyme B12 analogs and substrates. *J. Biol. Chem.* **285**, 26484–26493 (2010).

857 65. Mori, K., Bando, R., Hieda, N. & Toraya, T. Identification of a reactivating factor for
858 adenosylcobalamin-dependent ethanolamine ammonia lyase. *J. Bacteriol.* **186**, 6845–6854
859 (2004).

860 66. Costa, F. G. & Escalante-Semerena, J. C. Localization and interaction studies of the Salmonella
861 enterica ethanolamine ammonia-lyase (EutBC), its reactivase (EutA), and the EutT corrinoid
862 adenosyltransferase. *Mol. Microbiol.* **118**, 191–207 (2022).

863 67. Yang, M. *et al.* Molecular basis of the biogenesis of a protein organelle for ethanolamine
864 utilization. *bioRxiv* 2005–2024 (2024).

865 68. Sampson, E. M. & Bobik, T. A. Microcompartments for B12-dependent 1, 2-propanediol
866 degradation provide protection from DNA and cellular damage by a reactive metabolic
867 intermediate. *J. Bacteriol.* **190**, 2966–2971 (2008).

868 69. Dank, A. *et al.* Bacterial microcompartment-dependent 1, 2-propanediol utilization of
869 Propionibacterium freudenreichii. *Front. Microbiol.* **12**, 679827 (2021).

870 70. Moreira de Gouveia, M. I., Bernalier-Donadille, A. & Jubelin, G. Enterobacteriaceae in the
871 Human Gut: Dynamics and Ecological Roles in Health and Disease. *Biology (Basel).* **13**, 142
872 (2024).

873 71. Millard, P., Gosselin-Monplaisir, T., Uttenweiler-Joseph, S. & Enjalbert, B. Acetate is a
874 beneficial nutrient for E. coli at low glycolytic flux. *EMBO J.* e113079 (2023).

875 72. Heidrich, C. *et al.* Involvement of N-acetylmuramyl-L-alanine amidases in cell separation and
876 antibiotic-induced autolysis of Escherichia coli. *Mol. Microbiol.* **41**, 167–178 (2001).

877 73. Dailey, H. A. *et al.* The Escherichia coli protein YfeX functions as a porphyrinogen oxidase, not
878 a heme dechelatase. *MBio* **2**, 10–1128 (2011).

879 74. Bologna, F. P., Andreo, C. S. & Drincovich, M. F. Escherichia coli malic enzymes: two isoforms
880 with substantial differences in kinetic properties, metabolic regulation, and structure. *J.*
881 *Bacteriol.* **189**, 5937–5946 (2007).

882 75. Oh, M.-K., Rohlin, L., Kao, K. C. & Liao, J. C. Global expression profiling of acetate-grown
883 Escherichia coli∗. *J. Biol. Chem.* **277**, 13175–13183 (2002).

884 76. Rahman, M. & Shimizu, K. Altered acetate metabolism and biomass production in several
885 Escherichia coli mutants lacking rpoS-dependent metabolic pathway genes. *Mol. Biosyst.* **4**,
886 160–169 (2008).

887 77. Schürmann, M., Schürmann, M. & Sprenger, G. A. Fructose 6-phosphate aldolase and 1-deoxy-
888 D-xylulose 5-phosphate synthase from Escherichia coli as tools in enzymatic synthesis of 1-
889 deoxysugars. *J. Mol. Catal. B Enzym.* **19**, 247–252 (2002).

890 78. Jakobson, C. M., Tullman-Ercek, D., Slininger, M. F. & Mangan, N. M. A systems-level model
891 reveals that 1, 2-Propanediol utilization microcompartments enhance pathway flux through
892 intermediate sequestration. *PLoS Comput. Biol.* **13**, e1005525 (2017).

893 79. Mangan, N. M. & Brenner, M. P. Systems analysis of the CO2 concentrating mechanism in
894 cyanobacteria. *Elife* **3**, e02043 (2014).

895 80. Heldal, M., Norland, S. & Tumyr, O. X-ray microanalytic method for measurement of dry
896 matter and elemental content of individual bacteria. *Appl. Environ. Microbiol.* **50**, 1251–1257
897 (1985).

898 81. Clare, C., Rutter, J. W., Fedorec, A. J. H., Frank, S. & Barnes, C. P. Bacterial microcompartment
899 utilisation in the human commensal Escherichia coli Nissle 1917. *bioRxiv* 2005–2024 (2024).

900 82. Schindelin, J. *et al.* Fiji: an open-source platform for biological-image analysis. *Nat. Methods* **9**,
901 676–682 (2012).

902 83. Hagen, W. J. H., Wan, W. & Briggs, J. A. G. Implementation of a cryo-electron tomography tilt-
903 scheme optimized for high resolution subtomogram averaging. *J. Struct. Biol.* **197**, 191–198
904 (2017).

905 84. Mastronarde, D. N. Automated electron microscope tomography using robust prediction of
906 specimen movements. *J. Struct. Biol.* **152**, 36–51 (2005).

907 85. Kremer, J. R., Mastronarde, D. N. & McIntosh, J. R. Computer visualization of three-
908 dimensional image data using IMOD. *J. Struct. Biol.* **116**, 71–76 (1996).

909 86. Bepler, T., Kelley, K., Noble, A. J. & Berger, B. Topaz-Denoise: general deep denoising models

910 for cryoEM and cryoET. *Nat. Commun.* **11**, 5208 (2020).

911 87. Chen, M. *et al.* A complete data processing workflow for cryo-ET and subtomogram averaging.
912 *Nat. Methods* **16**, 1161–1168 (2019).

913 88. Pettersen, E. F. *et al.* UCSF ChimeraX: Structure visualization for researchers, educators, and
914 developers. *Protein Sci.* **30**, 70–82 (2021).

915 89. Bouyssié, D. *et al.* Proline: an efficient and user-friendly software suite for large-scale
916 proteomics. *Bioinformatics* **36**, 3148–3155 (2020).

917 90. Hodgetts, R. Y. *et al.* Refining universal procedures for ammonium quantification via rapid 1H
918 NMR analysis for dinitrogen reduction studies. *ACS Energy Lett.* **5**, 736–741 (2020).

919 91. Heuillet, M. *et al.* Methodology for the validation of isotopic analyses by mass spectrometry in
920 stable-isotope labeling experiments. *Anal. Chem.* **90**, 1852–1860 (2018).

921 92. Millard, P., Letisse, F., Sokol, S. & Portais, J.-C. IsoCor: correcting MS data in isotope labeling
922 experiments. *Bioinformatics* **28**, 1294–1296 (2012).

923 93. Peiro, C. *et al.* Chemical and metabolic controls on dihydroxyacetone metabolism lead to
924 suboptimal growth of Escherichia coli. *Appl. Environ. Microbiol.* **85**, e00768-19 (2019).

925 94. Ebrahim, A., Lerman, J. A., Palsson, B. O. & Hyduke, D. R. COBRApy: constraints-based
926 reconstruction and analysis for python. *BMC Syst. Biol.* **7**, 1–6 (2013).

927 95. Malik-Sheriff, R. S. *et al.* BioModels—15 years of sharing computational models in life science.
928 *Nucleic Acids Res.* **48**, D407–D415 (2020).

929 96. Millard, P., Enjalbert, B., Uttenweiler-Joseph, S., Portais, J.-C. & Létisse, F. Control and
930 regulation of acetate overflow in Escherichia coli. *Elife* **10**, e63661 (2021).

931 97. Millard, P., Portais, J.-C. & Mendes, P. Impact of kinetic isotope effects in isotopic studies of
932 metabolic systems. *BMC Syst. Biol.* **9**, 1–13 (2015).

933 98. Hoops, S. *et al.* COPASI—a complex pathway simulator. *Bioinformatics* **22**, 3067–3074 (2006).

934 **Figure legends:**

935 **Table 1. Bacterial strains and plasmids used in the study.**

936 **Table 2. Growth of *E. coli* K-12 W3110 strains grown in various M9 medium derivatives.** These
937 experiments were performed using a microplate reader. Data are shown as mean (n = 3 biological
938 replicates) ± standard deviation.

939 **Table 3. Growth parameters of *E. coli* K12 W3110 WT grown aerobically in M9 medium containing**
940 **glycerol as C source and NH_4Cl or EA as N source.** The exponential growth rate μ is expressed in h^{-1};
941 the substrate uptake (q_S) and product formation (q_P) rates are expressed in mmol.(gDW.h)$^{-1}$. DW: dry
942 weight; ND: not detected. Data are shown as mean (n = 3 biological replicates) ± standard deviation.

943 **Figure 1. The *eut* operon is essential for EA utilization as nitrogen source by *E. coli* K-12 W3110.** A)
944 Schematic representation of the chromosomal EUT1 locus in W3110 WT. Genes in grey flank the *eut*
945 operon and are conserved amongst the EUT1 loci of Beta- and Gammaproteobacteria. Genes with
946 other colours form the *eut* operon. Genes colored in yellow encode structural components of the Eut
947 BMC shell, those in blue code for enzymes (EA catabolism, coenzyme B12 biosynthesis) and those in
948 white encode other functions (chaperon, transporter). B) to E) Plate reader measurements of optical
949 density at 600 nm for strains grown in B) M9 medium containing glycerol (30 mM) as C source and

950 NH_4Cl (20 mM) as N source; C) M9 medium containing glycerol (30 mM) as C source and EA (20 mM)
951 as N source, including vitamin B12 (200 nM); D) M9 glycerol NH_4Cl with IPTG (20 µM) and E) M9 glycerol
952 EA vitamin B12 with IPTG (20 µM). All the strains and plasmids are described in Table 1. Gentamicin
953 (10 $\mu g.mL^{-1}$) was added for the plasmid-bearing strains. The data shown are from a representative
954 experiment of at least three independent replicates.

955 **Figure 2. The chimeric protein EutC-GFP forms disctinct puncta in EA-containing medium.** A)
956 Schematic representation of the $P_{LtetO-1}$::*eutC-GFP* expression cassette. This construct was inserted at
957 the *SS9* safe chromosomal locus in W3110 WT to produce W3110 *eutC-GFP*. B), C) and D)
958 Representative micrographs showing phase contrast images, GFP fluorescence signals, and composite
959 images from W3110 *eutC-GFP* grown in B) M9 glycerol NH_4Cl with 8 $ng.ml^{-1}$ aTc, C) M9 glycerol EA
960 vitamin B12 with 8 $ng.ml^{-1}$ aTc and D) M9 glycerol EA vitamin B12 with 80 $ng.ml^{-1}$ aTc. Scale bars
961 indicate 2 µm. E) Box plots indicating the number of GFP puncta per bacterium (n = 30 analyzed cells)
962 for cultures grown in M9 glycerol EA vitamin B12 with 8 $ng.ml^{-1}$ or 80 $ng.ml^{-1}$ aTc.

963 **Figure 3. *E. coli* K-12 W3110 produces well-formed Eut BMCs.** A) Representative electron
964 cryotomogram slice of W3110 WT grown in M9 glycerol EA vitamin B12 and B) Associated 3D
965 segmentation showing the cellular membranes in grey, the ribosomes in green, and the Eut BMCs in
966 blue. C) and D) Expanded views of Eut BMCs illustrating their variety in size and shape. The yellow
967 arrows in D) point towards possible cryoET (missing wedge) artefacts or partially assembled BMCs . E)
968 Representative tomogram slice of W3110 Δeut pEut_WT grown in M9 glycerol EA IPTG and F)
969 Associated segmentation. Scale bars indicate 100 nm.

970 **Figure 4. EA utilization requires minimal reorganization of the proteome.** Cultures were grown
971 aerobically in M9 glycerol EA vitamin B12 VS M9 glycerol NH_4Cl. Samples were collected for label-free
972 quantitative mass spectrometry-based proteomics analyses. A) Volcano plot with Eut proteins (fold
973 change > 2, $p < 0.05$) as red triangles, other upregulated proteins (fold change > 2, $p < 0.05$) as orange
974 squares, downregulated proteins (fold change < -2, $p < 0.05$) as blue triangles, and unaffected proteins
975 as black circles. B) Protein-protein interaction network as determined using STRING v11.5. Only
976 selected upregulated (white outline) and downregulated (black outline) proteins are shown. Thicker
977 lines indicate greater confidence in the considered protein-protein interactions. C) Normalized
978 abundance (IBAQ score) of Eut proteins in M9 glycerol EA vitamin B12, using EutQ as the reference.
979 Data shown are the mean of n = 4 biological replicates, bars correspond to standard deviations.

980 **Figure 5. The *E. coli* K12 W3110 Eut BMCs turn EA into usable C and N sources.** W3110 WT was grown
981 aerobically in M9 medium containing $^{12}C_3$-glycerol and $^{13}C_2$-EA. A) Biomass accumulation (grams dry
982 weight, gDW) and substrate consumption (mM); B) Product excretion. The substrates and products
983 were quantified by ^{1}H-NMR. Data shown are the average of n = 3 biological replicates, bars correspond
984 to standard deviations. C) Experimental and predicted fluxes through EA and glycerol metabolisms
985 using an isotopic model. Absolute flux values are summarized in Table S4. Blue-filled circles indicate
986 metabolites and green-filled rectangles indicate proteins. Unidentified sinks are indicated as barred
987 white circles. D) Carbon isotopologue distribution (CID) within proteinogenic aminoacids from biomass
988 samples harvested during exponential growth, showing the intracellular incorporation of ^{13}C derived
989 from EA. AAL: acetaldehyde; AcCoA: acetyl-CoA; Ace: acetate; AcP: acetyl-phosphate; EtOH: ethanol;
990 NH_4: ammonium.

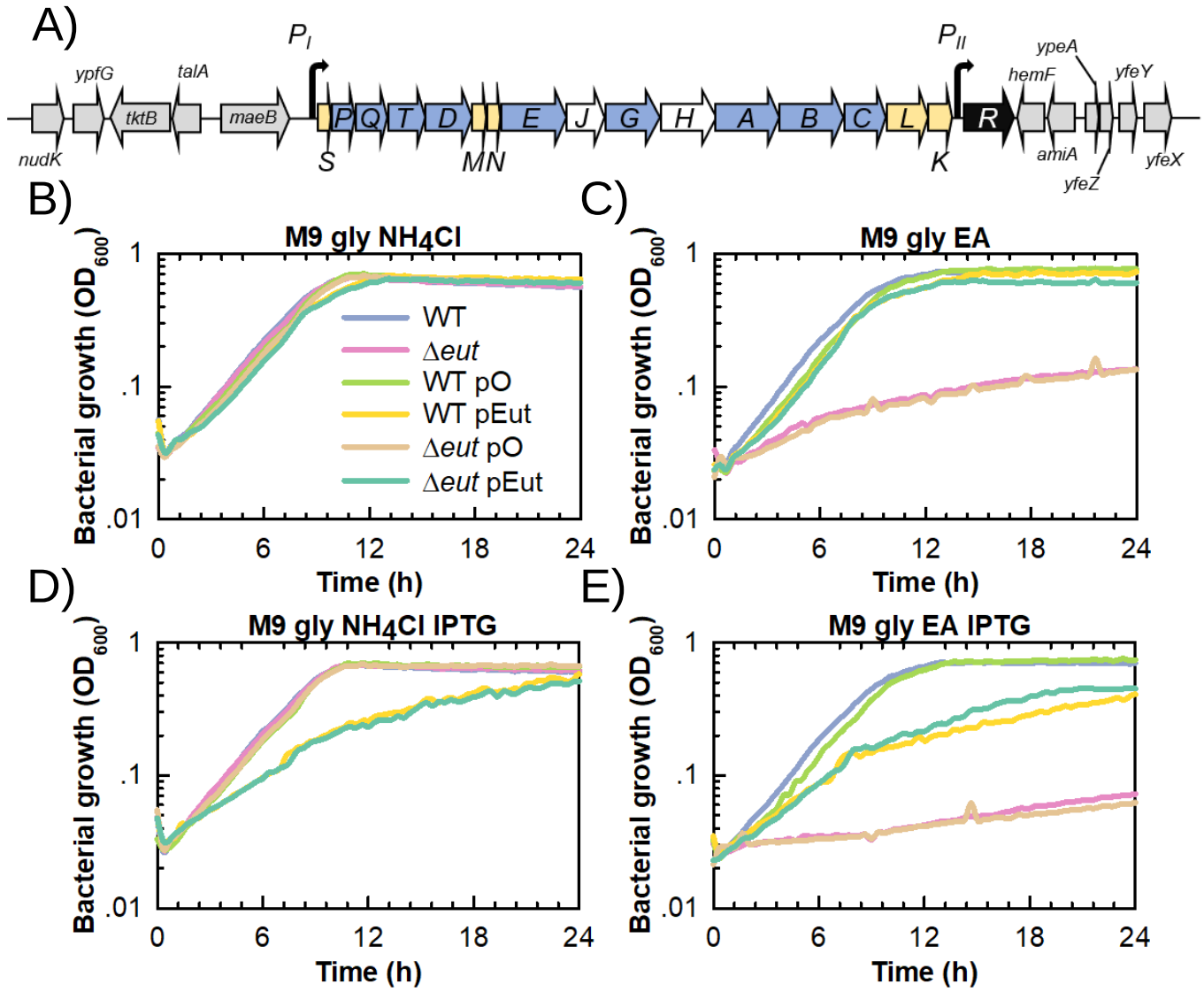

Figure 1. The *eut* operon is essential for EA utilization as nitrogen source by *E. coli* K-12 W3110. A) Schematic representation of the chromosomal EUT1 locus in W3110 WT. Genes in grey flank the *eut* operon and are conserved amongst the EUT1 loci of Beta- and Gammaproteobacteria. Genes with other colours form the *eut* operon. Genes colored in yellow encode structural components of the Eut BMC shell, those in blue code for enzymes (EA catabolism, coenzyme B12 biosynthesis) and those in white encode other functions (chaperon, transporter). B) to E) Plate reader measurements of optical density at 600 nm for strains grown in B) M9 medium containing glycerol (30 mM) as C source and NH_4Cl (20 mM) as N source; C) M9 medium containing glycerol (30 mM) as C source and EA (20 mM) as N source, including vitamin B12 (200 nM); D) M9 glycerol NH_4Cl with IPTG (20 µM) and E) M9 glycerol EA vitamin B12 with IPTG (20 µM). All the strains and plasmids are described in Table 1. Gentamicin (10 µg.mL^{-1}) was added for the plasmid-bearing strains. The data shown are from a representative experiment of at least three independent replicates.

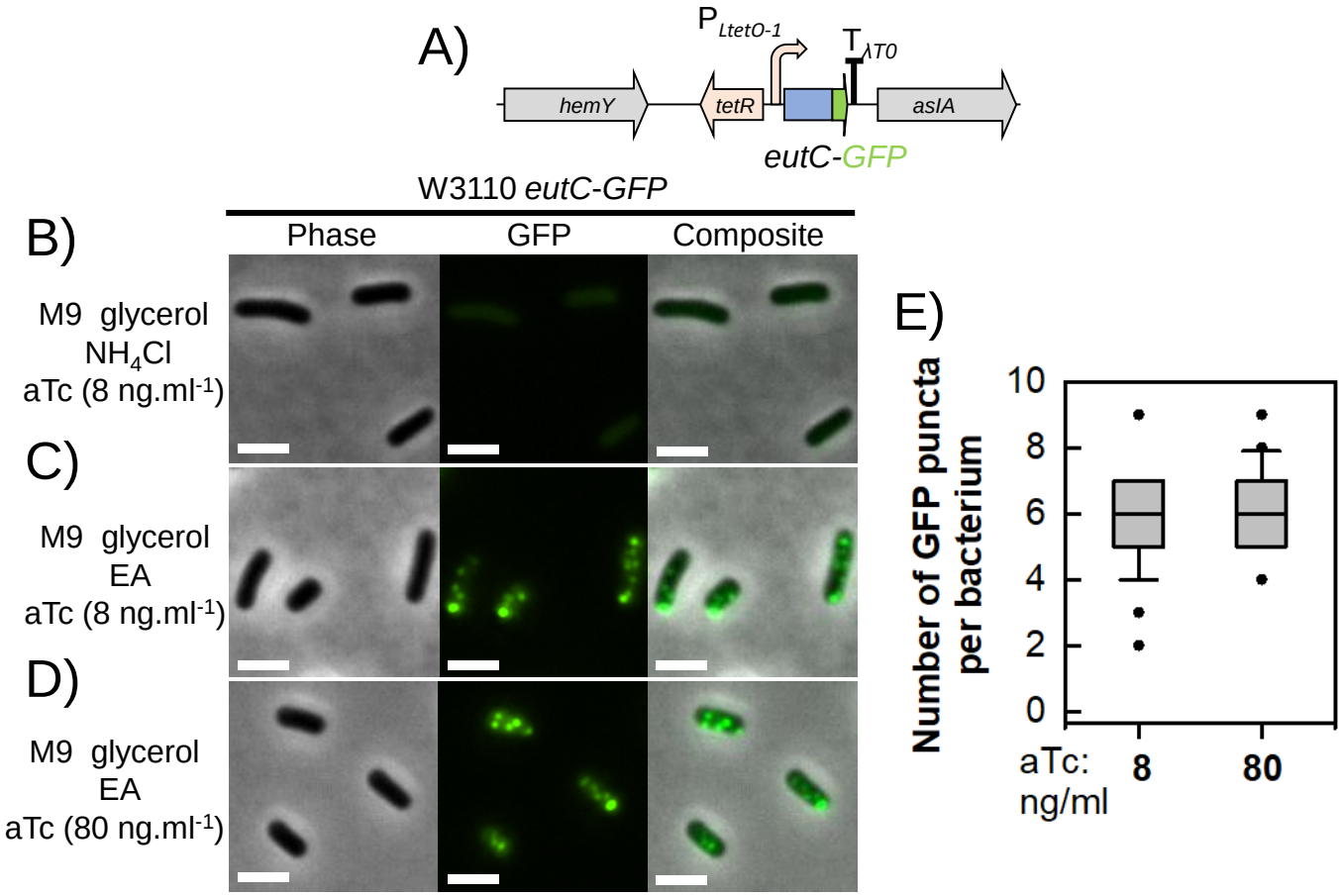

Figure 2. The chimeric protein EutC-GFP forms disctinct puncta in EA-containing medium. A) Schematic representation of the $P_{LtetO-1}$::*eutC-GFP* expression cassette. This construct was inserted at the *SS9* safe chromosomal locus in W3110 WT to produce W3110 *eutC-GFP*. B), C) and D) Representative micrographs showing phase contrast images, GFP fluorescence signals, and composite images from W3110 *eutC-GFP* grown in B) M9 glycerol NH_4Cl with 8 ng.ml^{-1} aTc, C) M9 glycerol EA vitamin B12 with 8 ng.ml^{-1} aTc and D) M9 glycerol EA vitamin B12 with 80 ng.ml^{-1} aTc. Scale bars indicate 2 µm. E) Box plots indicating the number of GFP puncta per bacterium (n = 30 analyzed cells) for cultures grown in M9 glycerol EA vitamin B12 with 8 ng.ml^{-1} or 80 ng.ml^{-1} aTc.

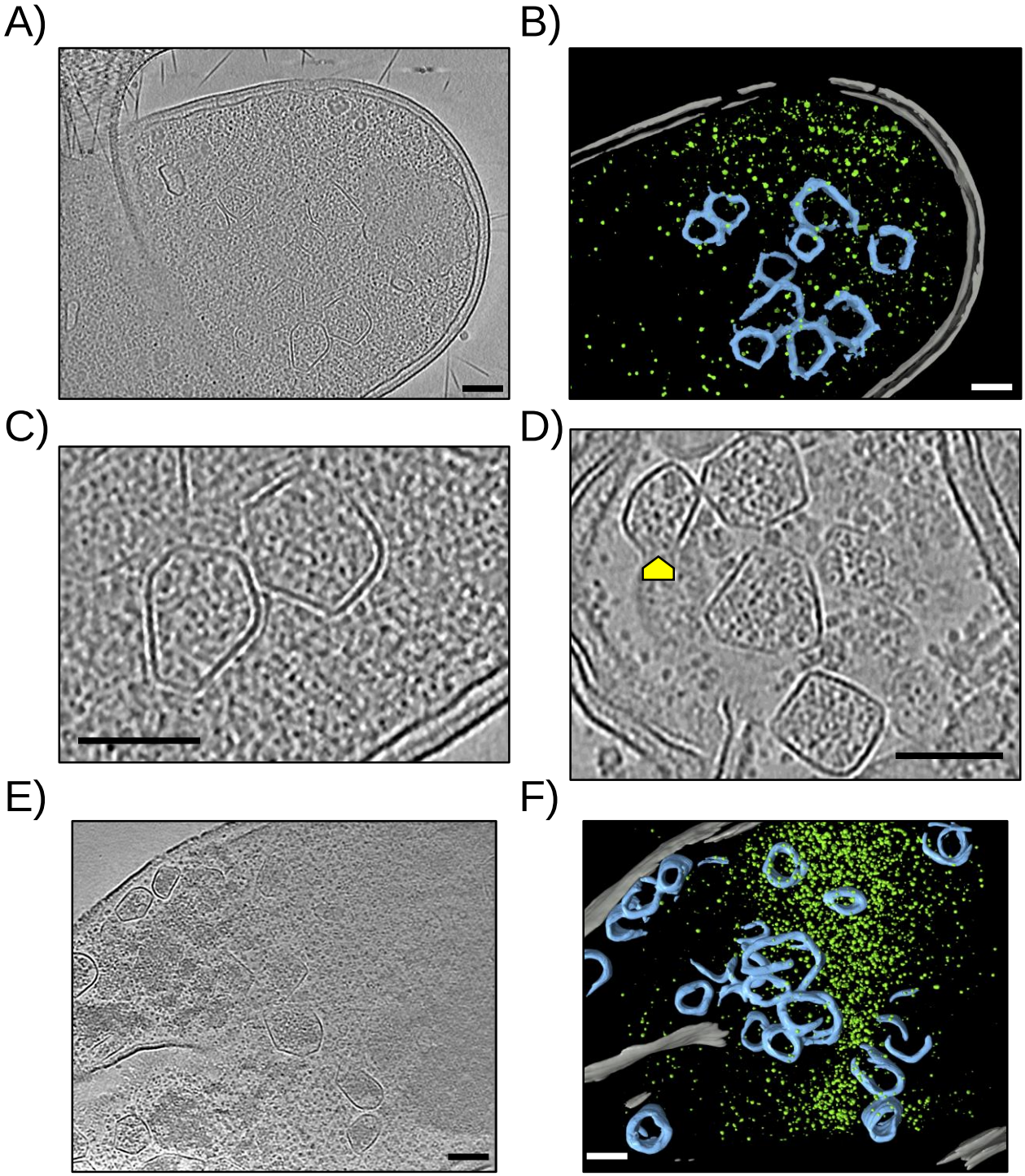

Figure 3. *E. coli* K-12 W3110 produces well-formed Eut BMCs. A) Representative electron cryotomogram slice of W3110 WT grown in M9 glycerol EA vitamin B12 and B) Associated 3D segmentation showing the cellular membranes in grey, the ribosomes in green, and the Eut BMCs in blue. C) and D) Expanded views of Eut BMCs illustrating their variety in size and shape. The yellow arrows in D) point towards possible cryoET (missing wedge) artefacts or partially assembled BMCs . E) Representative tomogram slice of W3110 Δeut pEut_WT grown in M9 glycerol EA IPTG and F) Associated segmentation. Scale bars indicate 100 nm.

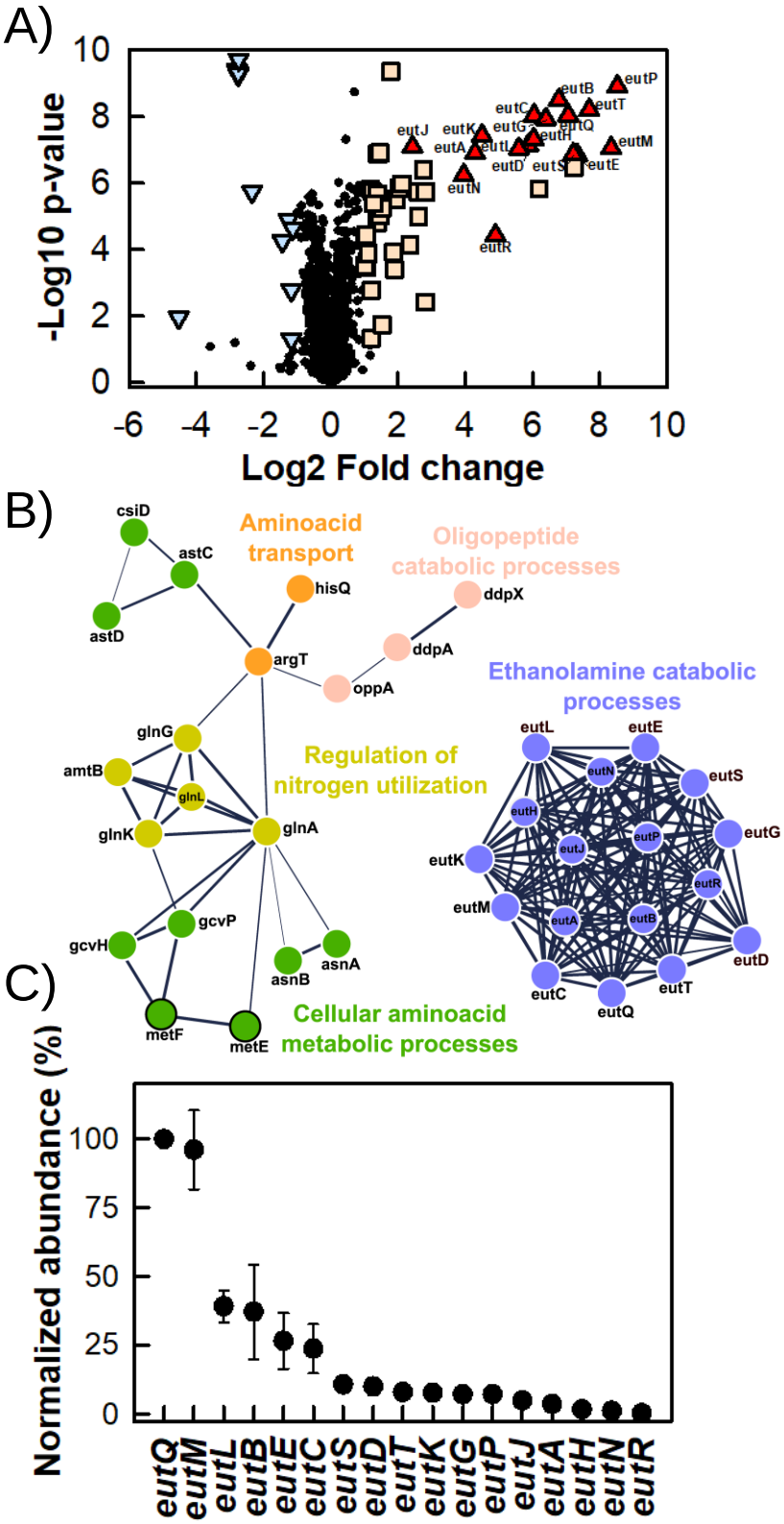

Figure 4. EA utilization requires minimal reorganization of the proteome. Cultures were grown aerobically in M9 glycerol EA vitamin B12 VS M9 glycerol NH_4Cl. Samples were collected for label-free quantitative mass spectrometry-based proteomics analyses. A) Volcano plot with Eut proteins (fold change > 2, $p < 0.05$) as red triangles, other upregulated proteins (fold change > 2, $p < 0.05$) as orange squares, downregulated proteins (fold change < -2, $p < 0.05$) as blue triangles, and unaffected proteins as black circles. B) Protein-protein interaction network as determined using STRING v11.5. Only selected upregulated (white outline) and downregulated (black outline) proteins are shown. Thicker lines indicate greater confidence in the considered protein-protein interactions. C) Normalized abundance (IBAQ score) of Eut proteins in M9 glycerol EA vitamin B12, using EutQ as the reference. Data shown are the mean of n = 4 biological replicates, bars correspond to standard deviations.

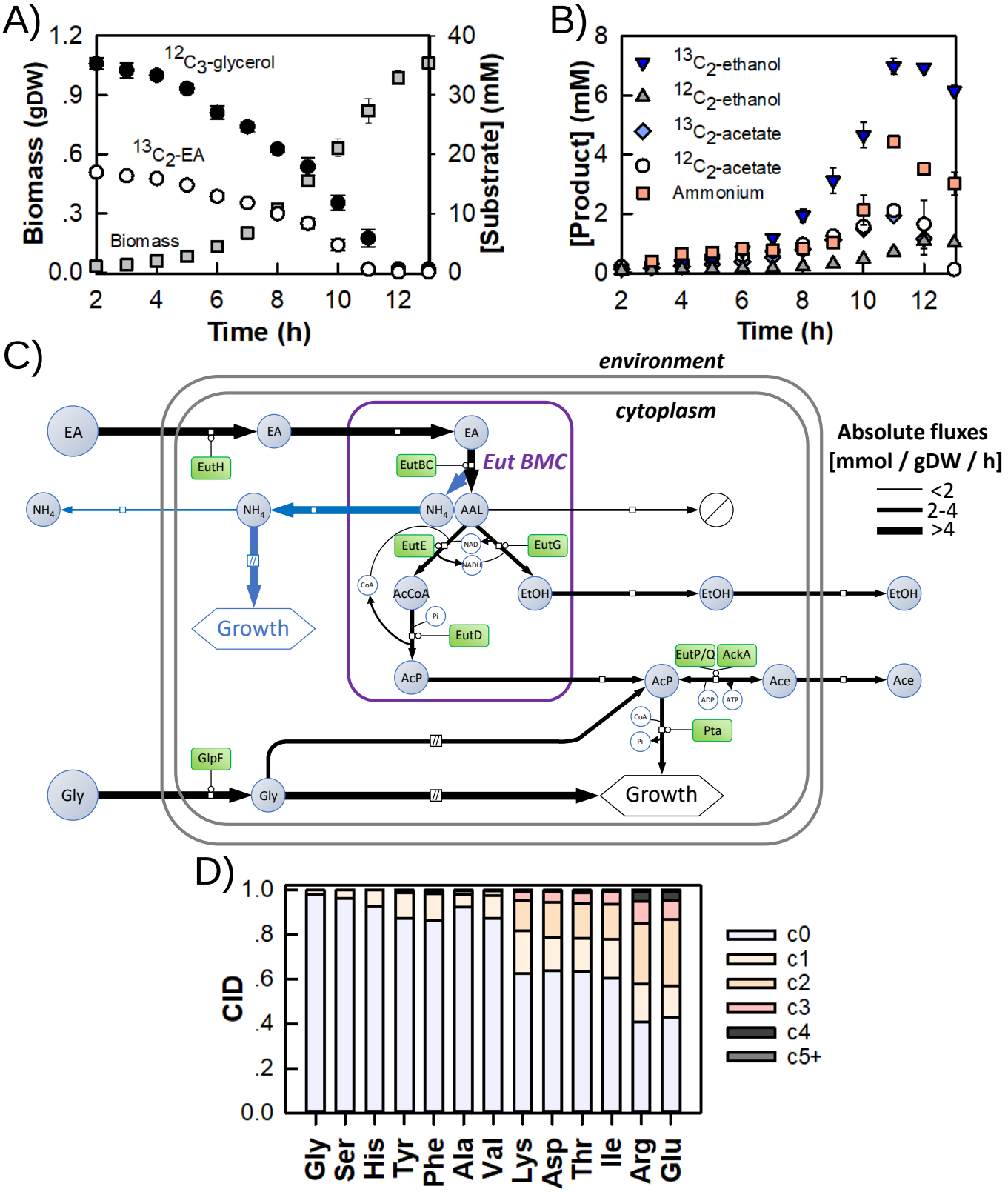

Figure 5. The *E. coli* K12 W3110 Eut BMCs turn EA into usable C and N sources. W3110 WT was grown aerobically in M9 medium containing $^{12}C_3$-glycerol and $^{13}C_2$-EA. A) Biomass accumulation (grams dry weight, gDW) and substrate consumption (mM); B) Product excretion. The substrates and products were quantified by ^{1}H-NMR. Data shown are the average of n = 3 biological replicates, bars correspond to standard deviations. C) Experimental and predicted fluxes through EA and glycerol metabolisms using an isotopic model. Absolute flux values are summarized in Table S4. Blue-filled circles indicate metabolites and green-filled rectangles indicate proteins. Unidentified sinks are indicated as barred white circles. D) Carbon isotopologue distribution (CID) within proteinogenic aminoacids from biomass samples harvested during exponential growth, showing the intracellular incorporation of ^{13}C derived from EA. AAL: acetaldehyde; AcCoA: acetyl-CoA; Ace: acetate; AcP: acetyl-phosphate; EtOH: ethanol; NH_4: ammonium.

Strains or plasmids	Genotype or description	Source
***E. coli* bacterial strains**		
W3110 WT	*E. coli* K-12 W3110 wild-type [F^- λ^- INV(*rrnD-rrnE*) *rph-1 eut*$^+$]	Laboratory collection
BW25113 WT	*E. coli* K-12 W3110 wild-type [F^- λ^- Δ*lacZ4787*(::*rrnB-3*) *hsdR514* Δ*(araBAD)567* Δ*(rhaBAD)568 rph-1 eut*$^-$(*:: cryptic prophage DNA*)]	Laboratory collection
W3110 Δ*eut*	Chromosomal *eut* operon removed by genome editing in W3110 WT	This study
BW25113 *eut*+	Cryptic prophage DNA insertion within the chromosomal *eut* operon removed by genome editing in BW25113 WT	This study
W3110 *eutC-GFP*	$P_{LtetO-1}$::*eutC-GFP* construct inserted at the SS9 safe chromosomal site in W3110 WT by genome editing	This study
W3110 *eutC*$_{1-20}$-*GFP*	$P_{LtetO-1}$::*eutC*$_{1-20}$-*GFP* construct inserted at the SS9 safe chromosomal site in W3110 WT by genome editing	This study
Plasmids		
pCas	*repA101*(Ts), *Kan*^{R}, P_{cas}::*cas9* P_{araB}::*Red lacIq* P_{trc}::*sgRNA-pMB1*	[22]
pTargetF	*pMB1*, *Sp*^{R}, *sgRNA-acs*; expression of a specific sgRNA to target *acs* in *E. coli*	[22]
pTargetF_eut	*pMB1*, Sp^R, sgRNA-*eutG*; pTargetF derivative for the expression of a specific sgRNA to target *eutG* in *E. coli*	This study
pHD_Δ*eut*	*pUC*, Amp^R, contains the 1kb-long upper and lower homology arms required to knock out the chromosomal *eut* operon in W3110 WT	This study
pTargetF_SS9	*pMB1*, Sp^R, sgRNA-*SS9*; pTargetF derivative for the expression of a specific sgRNA to target the *SS9* locus in *E. coli*	This study
pHD_SS9_eutC-GFP	*pUC*, Amp^R, contains 1kb-long homology regions to insert the $P_{LtetO-1}$::*eutC-GFP* construct at the SS9 safe chromosomal site in W3110 WT	This study
pHD_SS9_eutC$_{1-20}$-GFP	*pUC*, Amp^R, contains 1kb-long homology regions to insert the $P_{LtetO-1}$::*eutC*$_{1-20}$-*GFP* construct at the SS9 safe chromosomal site in W3110 WT	This study
pSEVA661	*p15A*, Gm^R	[24]
pO	*lacI*$_Q$-P_{trc} cassette and T_0 terminator cloned into the multiple cloning site of pSEVA 661	This study
pEut	Entire *eut* operon from W3110 WT cloned into pO under control of P_{trc}	This study

Table 1. Bacterial strains and plasmids used in the study.

	μ_{max} (h^{-1})			
Strain/Medium	**M9 glycerol NH_4Cl**	**M9 glycerol NH_4Cl IPTG**	**M9 glycerol EA**	**M9 glycerol EA IPTG**
WT	0,37 ± 0,01	0,37 ± 0,01	0,39 ± 0,01	0,39 ± 0,01
Δ*eut*	0,36 ± 0,03	0,35 ± 0,01	0,09 ± 0,06	0,03 ± 0,02
WT pO	0,35 ± 0,01	0,36 ± 0,01	0,38 ± 0,03	0,35 ± 0,01
WT pEut	0,33 ± 0,01	0,19 ± 0,01	0,37 ± 0,01	0,23 ± 0,01
Δeut pO	0,35 ± 0,01	0,35 ± 0,01	0,12 ± 0,11	0,02 ± 0,01
Δ*eut* pEut	0,33 ± 0,01	0,19 ± 0,01	0,37 ± 0,01	0,25 ± 0,01

Table 2. Growth of *E. coli* K-12 W3110 strains grown in various M9 medium derivatives. These experiments were performed using a microplate reader. Data are shown as mean (n = 3 biological replicates) ± standard deviation.

	Physiological parameters				
Medium	**μ**	**$q_{S)glycerol}$**	**$q_{S)Ethanolamine}$**	**$q_{P)acetate}$**	**$q_{P)ethanol}$**
M9 gly NH_4Cl	0.44 ± 0.02	16.2 ± 1.6	ND	ND	ND
M9 gly EA	0.45 ± 0.01	14.7 ± 0.4	7.8 ± 0.3	1.7 ± 0.1	2.6 ± 0.1

Table 3. Growth parameters of *E. coli* K12 W3110 WT grown aerobically in M9 medium containing glycerol as C source and NH_4Cl or EA as N source. The exponential growth rate μ is expressed in h^{-1}; the substrate uptake (q_S) and product formation (q_P) rates are expressed in mmol.(gDW.h)$^{-1}$. DW: dry weight; ND: not detected. Data are shown as mean (n = 3 biological replicates) ± standard deviation.